Late Quaternary chronostratigraphic framework of deep Baffin Bay glaciomarine sediments from high-resolution paleomagnetic data

Quentin Simon, Guillaume St-onge, Claude Hillaire-marcel

Geochemistry Geophysics Geosystems G3

Article
Volume 13, Number 1
7 November 2012
Q0AO03, doi:10.1029/2012GC004272
ISSN: 1525-2027

Published by AGU and the Geochemical Society

Late Quaternary chronostratigraphic framework of deep Baffin Bay glaciomarine sediments from high-resolution paleomagnetic data

Quentin Simon
Geotop Research Centre, Université du Québec à Montréal, Montréal, Quebec H3C 3P8, Canada (quentin.simon@gmx.com)

Guillaume St-Onge
Canada Research Chair in Marine Geology, Institut des sciences de la mer de Rimouski, Université du Québec à Rimouski, Rimouski, Quebec G5L 3A1, Canada

Geotop Research Centre, Montréal, Quebec H3C 3P8, Canada

Claude Hillaire-Marcel
Geotop Research Centre, Université du Québec à Montréal, Montréal, Quebec H3C 3P8, Canada

[1] The late Quaternary Baffin Bay sediments provide exclusive records of Greenland, Innuitian and Laurentide ice sheet margin activities, as well as information about the Arctic and northern Atlantic ocean linkages through the Canadian Arctic Archipelago. Because of specific oceanographic conditions, foraminiferal δ^{18}O-stratigraphies and radiocarbon ages fail to provide reliable chronologies. Here we propose an original chronostratigraphy spanning the last glacial cycle based on high-resolution paleomagnetic investigations on a 741-cm long core (HU2008-029-016PC) raised from the deep central Baffin Bay, near ODP site 645. Two major difficulties were encountered: (1) the high-frequency occurrence of rapidly deposited layers related to short ice sheet margin events (e.g., ice surges), and (2) the magnetic grain size variability. Physical and magnetic mineralogical properties were used to screen out unreliable magnetic sediment layers. The obtained relative paleointensity (RPI) proxy matches reference paleomagnetic stacks and regional records. Moreover, the resulting record depicts two major excursions which were assigned to the Laschamp and the Norwegian-Greenland-Sea events. It has thus been possible to derive a robust 115 ka chronology for the cored sequence. We concluded that even under such a dynamic sedimentary regime, magnetic properties of the sediments can provide a reliable chronostratigraphy, together with information on sedimentary processes.

Components: 13,100 words, 12 figures, 2 tables.

Keywords: Baffin Bay; chronostratigraphy; geomagnetic excursions; late Quaternary; paleointensity; rock magnetism.

Index Terms: 1513 Geomagnetism and Paleomagnetism: Geomagnetic excursions; 1521 Geomagnetism and Paleomagnetism: Paleointensity; 1540 Geomagnetism and Paleomagnetism: Rock and mineral magnetism.

Received 4 June 2012; **Revised** 27 September 2012; **Accepted** 28 September 2012; **Published** 7 November 2012.

Simon, Q., G. St-Onge, and C. Hillaire-Marcel (2012), Late Quaternary chronostratigraphic framework of deep Baffin Bay glaciomarine sediments from high-resolution paleomagnetic data, *Geochem. Geophys. Geosyst.*, *13*, Q0AO03, doi:10.1029/2012GC004272.

Theme: Magnetism From Atomic to Planetary Scales: Physical Principles and Interdisciplinary Applications in Geo- and Planetary Sciences

1. Introduction

[2] The Baffin Bay area constitutes a unique vantage point to study the ice margin dynamics of several of the largest late Quaternary ice sheets (i.e., Laurentide, Innuitian and Greenland). However, paleoceanographic studies in Baffin Bay, and more largely in the Arctic basins, have been proven highly challenging due to chronostratigraphic limitations. Biogenic carbonates are either scarce or dissolved in the terrigenous glaciomarine sediments of the central Baffin Bay, thus preventing the setting of reliable ^{14}C-chronologies or oxygen isotope stratigraphies [*Aksu*, 1981; *de Vernal et al.*, 1987; *Srivastava et al.*, 1989; *Andrews et al.*, 1998]. In addition, the production of isotopically light brines resulting from sea-ice formation often hinders the interpretation of foraminiferal oxygen isotope data when they exist [*Hillaire-Marcel et al.*, 2004; *Hillaire-Marcel and de Vernal*, 2008].

[3] As a consequence, ambiguous and conflicting late Quaternary chronostratigraphies have been proposed for central Baffin Bay sediments. (1) *Aksu and Piper* [1979] proposed a chronology involving relatively high sedimentation rates (8–12 cm/ka) based on the identification of ash horizons and peaks of foraminifera abundance. (2) Later, *Aksu* [1983a] and *Mudie and Aksu* [1984] revisited this model and proposed a chronology presenting lower sedimentation rates (2–3 cm/ka) based on bulk ^{14}C dates and δ^{18}O interpretations. According to this chronology, *Aksu* [1983b] assigned a geomagnetic excursion recorded between 2.5 and 4.5 mbsf in Baffin Bay cores raised during the 1970s to the Blake event ($\sim$123 $\pm$ 3 ka BP) [*Lund et al.*, 2006]. (3) Later on, *de Vernal et al.* [1987] presented new ^{14}C ages on foraminifera and dinocyst assemblages' interpretation that favored the high sedimentation rate scenario (8–12 cm/ka). (4) Magnetostratigraphic investigations carried out on Ocean Drilling Program (ODP) site 645 set the Brunhes/Matuyama boundary at 90 mbsf, thus in support of a mean sedimentation rate of 12 cm/ka [*Baldauf et al.*, 1989]. (5) *Thouveny* [1988] identified 2 intervals with anomalous inclinations possibly confirming the high sedimentation rate hypothesis (notably the possible recognition of the Mono Lake excursion around 2.5 mbsf, yielding a mean sedimentation rate of 10 cm/ka). In *Thouveny*'s [1988] study, two radiocarbon ages even suggested a higher sedimentation rate during MIS2 ($\sim$20 cm/ka). (6) Finally, *Andrews et al.* [1998] reviewed the chronology in central Baffin Bay based on 21 new AMS ^{14}C ages in 9 piston cores from central Baffin Bay [*Aksu*, 1981]. They proposed a temporal correlation between Baffin Bay Detrital Carbonate layers (BBDC) and the onset of major interstadial δ^{18}O peaks recorded in the GISP2 ice core. That assumption ruled out the low sedimentation rate hypothesis. Thus, although the stratigraphy of Baffin Bay sediment is now better constrained (e.g., more radiocarbon ages, lithofacies, BBDC), the "climatostratigraphic" interpretations of deep-sea cores remain largely imprecise and insufficient to resolve the phase relationships between millennial-scale climate records.

[4] Magnetic stratigraphy constitutes a valuable answer to resolve these chronological issues in such environments although some conditions have to be achieved to obtain reliable records [e.g., *Tauxe*, 1993; *Tauxe and Yamazaki*, 2007; *Valet*, 2003; *Stoner et al.*, 1998, 2000; *Stoner and St-Onge*, 2007; *St-Onge and Stoner*, 2011; *Channell et al.*, 1997, 2002, 2009; *Xuan and Channell*, 2010]. In this paper, we revisit previous age model hypotheses and present an original age model for central Baffin Bay based on the combination of relative paleointensity (RPI) data, the identification of magnetic excursions and radiocarbon dating.

2. Regional Setting

2.1. Hydrography

[5] Baffin Bay (Figure 1) is a narrow oceanic basin (1300 km long and 450 km wide, $\sim$690 000 km^2) nearly enclosed with shallow connections to the Arctic by Nares Strait and the Canadian Arctic Archipelago (CAA) channels, and a connection to the North Atlantic via Davis Strait (sill depth: 650 m). The morphology of the bay consists of a central abyssal plain (2000–2500 m) surrounded by continental shelves (Figure 1). Surface current circulation is anti-clockwise [*Tang et al.*, 2004] (Figure 1). The modern specific oceanographic features of the bay lead to a very shallow lysocline resulting in poor preservation of calcareous microfossils [*Aksu*, 1983a; *de Vernal et al.*, 1992; *Azetsu-Scott et al.*, 2010]. Extensive sea-ice covers the bay except in August and September and does not allow for high productivity rates [*Tang et al.*, 2004].

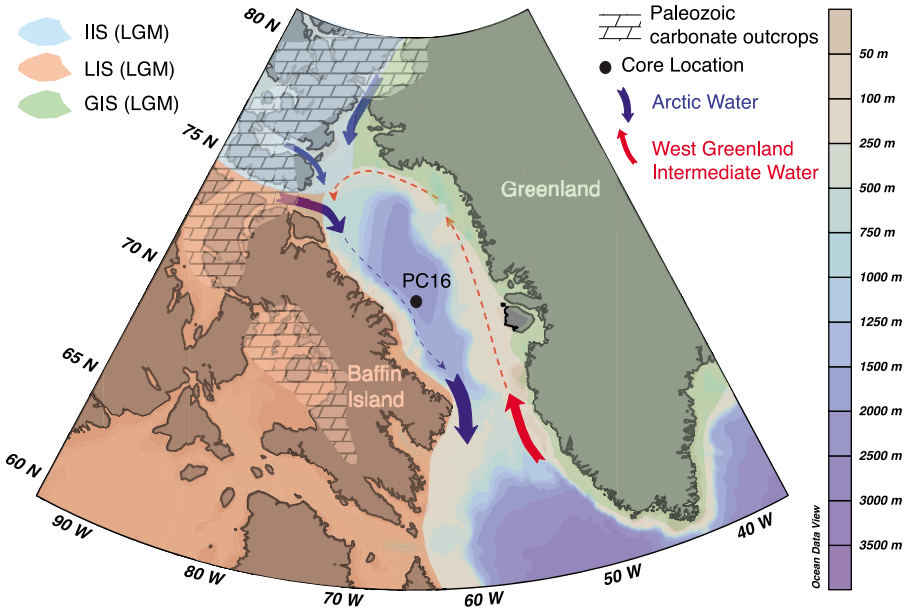

Figure 1. Map of the Baffin Bay area and location of core HU2008-029-016PC sampling site. The general bathymetry, simplified oceanic circulation and a sketch of the Paleozoic outcrops North of Davis Strait [*MacLean*, 1985] are also represented. Red arrows illustrate Atlantic "warm" waters, whereas the blue arrows represent colder Arctic waters. The simplified representation of the regional ice sheets extent limits during the LGM (colored areas) are adapted from *Funder et al.* [2011], *Dyke* [2004] and *England et al.* [2006]. IIS represents the Innuitian Ice Sheet, LIS represents the Laurentide Ice Sheet, and GIS represents the Greenland Ice Sheet.

2.2. Bedrock Geology

[6] The Baffin Bay geology is mostly characterized by a Precambrian crystalline basement overlain by a Lower Paleozoic succession dominated by shallow marine platform carbonates. Very limited outcrops of younger rocks are found. Tertiary rifting resulted in the development of a series of large grabens (sound, strait) and basaltic flows, observed along Canadian and Greenland Precambrian Shield margins [*Hiscott et al.*, 1989; *Korstgård and Nielsen*, 1989; *Thiébault et al.*, 1989; *Aksu and Piper*, 1987; *MacLean et al.*, 1990]. Archean and Paleoproterozoic are the largest outcropping units on each side of the bay. Paleozoic carbonate, principally dolostones with some limestones, outcrops in NW Greenland and the Canadian Arctic Archipelago (Figure 1).

2.3. Quaternary Geology and Sedimentation

[7] During the Last Glacial Maximum (LGM) the NE Laurentide Ice Sheet (LIS), the Innuitian Ice Sheet (IIS) and the western Greenland Ice Sheet (GIS) constituted a continuous ice belt surrounding Baffin Bay. The GIS probably extended westward at the inner shelf, and possibly as far as the shelf edge [*O'Cofaigh et al.*, 2010; *Funder et al.*, 2011]. GIS and IIS were likely joined across Nares Strait [*England et al.*, 2006]. The LIS extended through Baffin Island, probably as far as the fjords mouths and possibly over part of the Baffin Island shelf [*Briner et al.*, 2003, 2006]. Deglaciation was on its way as early as ~15–16 cal ka BP [*Briner et al.*, 2006; *Funder et al.*, 2011; *Jennings et al.*, 2011]. However, Nares Strait was not deglaciated until 8.5 cal ka BP [*Dyke*, 2004; *Jennings et al.*, 2011].

[8] The impact of the pre-LGM glaciations on Baffin Bay sediment delivery is poorly known because of weak chronostratigraphies [*Vincent and Prest*, 1987]. Nevertheless, sedimentary facies and the mineralogy of the late Quaternary sediments have been thoroughly described [e.g., *Marlowe*, 1966; *Piper*, 1973; *Aksu*, 1981; *Aksu and Piper*, 1987; *Hiscott et al.*, 1989; *Andrews et al.*, 1998]. Based on the mineralogy of detrital supplies and sediment textures, sedimentary processes were tightly controlled by glacial/interglacial (or stadial/interstadial) cycles and sediment facies could be discriminated from their deposition processes. For instance, deposition of coarser carbonate (dolomite-rich) ice-rafted sediments (i.e., Baffin Bay Detrital Carbonates layers, BBDC) suggest an axial source of ice-rafted debris, probably reflecting rapid breakup and melting of formerly dry-base ice shelves off Devon and Ellesmere Islands and in Lancaster Sound [*Aksu and Piper*, 1987; *Parnell et al.*, 2007].

According to *Andrews et al.* [1998], these BBDC layers may be broadly coeval with major interstadials $\delta^{18}O$ peaks of the GISP2 record and could be caused by or associated with the inflow of warm Atlantic Water into the western part of the bay [*Hiscott et al.*, 1989; *Andrews et al.*, 1998] causing rapid retreat of northern Baffin Bay ice streams. However, the age models and timing for these BBDC-events are insufficient to properly correlate them with Greenland interstadials or North Atlantic Heinrich events as well as to put forwards unquestionable relationships between both types of events.

3. Materials and Methods

[9] Core HU2008-029-016PC (PC16 hereinafter) is a 741-cm long piston core raised from central Baffin Bay during the 2008-029 CCGS Hudson expedition (70°46.14 N/−64°65.77 W; water depth: 2063 m) [*Campbell and de Vernal*, 2009]. The core location (Figure 1) is within proximity of an ODP site previously drilled in 1985 (ODP 645, leg 105) [*Srivastava et al.*, 1989] and of several sites of cores raised from deep central Baffin Bay during the 1970s and 1980s [*Aksu*, 1981; *Aksu and Piper*, 1987; *Andrews et al.*, 1998].

3.1. Physical and Geochemical Properties

[10] Physical properties such as wet bulk density (by Gamma Ray Attenuation) and low field volumetric magnetic susceptibility (k_{LF}) were measured on board using a GEOTEK Multi Sensor Core Logger (MSCL) at 1 cm intervals. Diffuse spectral reflectance data were acquired at 1 cm resolution immediately after splitting the core, using a Minolta CM-2600d handheld spectrophotometer and then converted into the *Commission Internationale de l'Eclairage* (CIE) color space (i.e., L*, a*, b*) [*St-Onge et al.*, 2007]. The core sections (1.5 m long) were described and sampled with u-channels (rigid u-shaped plastic liners, 2 × 2 cm cross section) from the center of the working halves for paleomagnetic and μXRF (ITRAX™ core scanner-see below) analyses. The archive halves were ran through a computerized coaxial tomography scanner (CAT-Scan) at 0.1 cm intervals at INRS-ETE in Québec City. The digital X-ray resulting images were displayed on gray scale and expressed as CT numbers, which primarily reflects changes in bulk density [*St-Onge et al.*, 2007; *Duchesne et al.*, 2009]. Grain size analyses were performed on sediment samples (1–2 g) at the *Institut des sciences de la mer de Rimouski* (ISMER) using a Beckman Coulter™ LS13320 laser diffraction grain size analyzer at 4 cm intervals. Wet sediment was mixed in a solution of 20 gL^{-1} of Calgon electrolytic solution (sodium hexametaphosphate) and water. The samples were rotated for 3 h and then sieved at 2 mm prior to analysis. The grain size distribution and statistical parameters (mean, standard deviation) were calculated using the Gradistat software [*Blott and Pye*, 2001]. Relative content of calcium (Ca), titanium (Ti), iron (Fe), manganese (Mn), among others, were determined by micro X-ray fluorescence (μXRF) spectrometry on the u-channels at 0.5 cm intervals and a 50 s counting time using an ITRAX™ core scanner (Cox Analytical Systems). The measurements were carried out at the GIRAS laboratory (Geochemistry, Imagery and Radiography of Sediment) of INRS-ETE, with a molybdenum anode tube that allowed the measurements of elements from Si to U. The output data represent relative concentrations, which are reported in peak area integrals for each element (dispersive energy spectrum). Ca contents were used to identify the BBDC layers in core PC16 assuming Ca was of detrital origin [*Polyak et al.*, 2009].

3.2. Mineralogy

[11] Mineralogical assemblages were determined by X-ray diffraction (XRD) at UQAM using a Siemens D-5000 diffractometer (CoKα1,2 radiation and a Si detector). The analyses were performed on bulk sediments (<2 mm) from the top of the core to 115 cm at 4 cm intervals. Semiquantitative estimations ($\pm 1\sigma$ ~5%) of the main mineral species were based on the height of the first diffraction peak for each mineral corrected for quartz [*Thorez*, 2003].

3.3. Magnetic Remanence Analyses

[12] Paleomagnetic data were measured at the *Laboratoire de paléomagnétisme sédimentaire et géologie marine* at ISMER with a 2G-Enterprises™ u-channel cryogenic magnetometer allowing the continuous measurement, at 1 cm intervals, of the natural, anhysteretic and isothermal remanent magnetizations (respectively NRM, ARM, IRM). The response function of the magnetometer pick-up coils integrates measurements over several centimeters (~7–8 cm). To reduce the edge effect associated with the response function, the data from the last and first 5 cm of each u-channel were excluded. The NRM was measured using stepwise alternating field (AF) demagnetization at peak fields from 0 to 80 mT at 5 mT increments. Directions (inclination and declination) of the characteristic remanent magnetization (ChRM) were calculated

Table 1. Radiocarbon Ages for Core HU2008-029-016PC

Depth (cm)	^{14}C Age[a] (yr BP)	ΔR	Calibrated Age[b] (cal BP)	Dated Material[c]	Laboratory Number[d]
66–67	11905 ± 40	0	13355 (13254–13457)	planktonic foraminifera (Npl)	CAMS-151299
		400	12953 (12783–13124)		
79–80	12470 ± 40	0	13859 (13738–13981)	planktonic foraminifera (Npl)	CAMS-151297
		400	13525 (13372–13678)		
111–112	13820 ± 130	0	16361 (15835–16888)	planktonic foraminifera (Npl)	CAMS-151300
		400	15783 (15109–16458)		

[a]The age was determined by the AMS method and corrected for natural and sputtering fractionation ($\delta^{13}C$ = ~25% versus Vienna Pee-Dee Belemnite (VPDB)). The statistical uncertainty of the age determination is given as one standard deviation [*Stuiver and Polach*, 1977].
[b]Calibrated using the CALIB 6.0 software [*Stuiver et al.*, 2010] using the *Hughen et al.* [2004] marine data set. A total marine reservoir correction of 400 yr (ΔR = 0 yr) and 800 yr (ΔR = 400 yr) were applied. The first and last ages, in parentheses, represent the 2σ cal age range.
[c]Npl = *Neogloboquadrina pachyderma* left-coiled.
[d]Center for Accelerator Mass Spectrometry, Lawrence Livermore National Laboratory.

by principal component analysis (PCA) with 9 AF demagnetization steps from 20 to 60 mT. The declination record was rotated in order to adjust the mean declination to zero. The precision of the best fit procedure was estimated by the maximum angular deviation (MAD) [*Kirschvink*, 1980]. MAD values lower than 5° are often considered as high quality directional data for paleomagnetic secular variations (PSV) and relative paleointensity (RPI) studies of Quaternary marine sediments [*Stoner and St-Onge*, 2007]. The ARM was induced at a peak AF of 100 mT with a 0.05 mT direct current (DC) biasing field, and then demagnetized and measured from 0 mT to 70 mT at 5 mT increments. The ARM was also expressed as the anyhsteretic susceptibility (k_{ARM}) by normalizing the ARM with the biasing field. An IRM was imparted to the z axis of the u-channel with a DC pulse field of 0.3 T using a 2G Enterprises™ pulse magnetizer. The IRM was then demagnetized and measured from 0 mT to 70 mT at 5 mT increments. A second IRM corresponding to a saturated IRM (SIRM) was imparted with a higher DC field of 0.95 T and then demagnetized and measured at the same steps. We calculated the IRM/SIRM ratio (Pseudo-S ratio) after AF demagnetization at peak fields of 25 mT in order to measure the relative importance of the high coercivity component of the magnetic mineral assemblage [e.g., *Stoner and St-Onge*, 2007]. Values close to 1 are indicative of low coercivity magnetic carriers (e.g., magnetite), whereas lower values indicate a high coercivity magnetic mineralogy (e.g., hematite). Median destructive field (MDF, the value of the peak AF necessary to reduce the magnetic remanence to half of its initial value) of the NRM was calculated using the Mazaud Excel spreadsheet [*Mazaud*, 2005]. It reflects the mean coercivity state of the magnetic grain assemblage, which depends on both the grain size and mineralogy [e.g., *Dunlop and Özdemir*, 1997; *Dankers*, 1981]. The k_{ARM}/k_{LF} ratio was calculated to estimate the magnetic grain size variability throughout the core [*Banerjee et al.*, 1981; *King et al.*, 1982; *Maher and Thompson*, 1999].

3.4. Rock Magnetism

[13] Magnetic assemblages were determined in 170 samples by measuring hysteresis properties, back-field remanence and IRM acquisition curves using an alternating gradient force magnetometer (AGM) MicroMag™ 2900 from Princeton Measurements Corporation™. Hysteresis loops along with backfield remanence curves were used to determine saturation magnetization (Ms), coercive force (Hc), saturation remanence (Mrs) and coercivity of remanence (Hcr). The ratios Mrs/Ms and Hcr/Hc are used as magnetic grain size proxies and to identify the magnetic domain state [*Day et al.*, 1977; *Dunlop*, 2002a; *Tauxe et al.*, 1996; *Tauxe*, 2010]. In a biplot of these ratios, theoretical area for single (SD), pseudo-single (PSD) and multi domain (MD) magnetite grains and the mixing reference curves have been proposed by *Day et al.* [1976] and then revisited by *Dunlop* [2002a, 2002b]. Along with these measurements, the temperature-dependence of magnetic susceptibility was measured on 24 samples using a MS2WF Bartington™ instrument. The measurements were made at 2°C steps from room temperature (~24°C) to 700°C and subsequent cooling to room temperature (air environment). The magnetic mineralogy can be determined using the specific Curie temperature of minerals [*Dunlop and Özdemir*, 1997].

3.5. Radiocarbon Dating

[14] Three radiocarbon ages were obtained (Table 1) from planktonic foraminifera (*Neogloboquadrina*

pachyderma left-coiled (Npl)) samples by accelerator mass spectrometry measurements performed at the Lawrence Livermore National Laboratory Center for Accelerator Mass Spectroscopy (LLNL-CAMS). The ^{14}C ages were then calibrated using the CALIB 6.0 software [*Stuiver et al.*, 2010] using the Marine09 data set [*Reimer et al.*, 2009]. Results are reported in calendar *kilo*-years before present (cal ka BP) at the 2σ-confidence level (95%) (Table 1). A regional reservoir correction of 0 yr ($\Delta R = 0$) was first applied based on ocean circulation and ventilation similar to today [*Coulthard et al.*, 2010]. However, ΔR values during the last deglaciation, i.e., the interval dated here, probably departed from 0 yr. Therefore, we applied the Bayesian calibration technique using the BCal online program (C. E. Buck, J. A. Christen, and G. N. James, BCal: An on-line Bayesian radiocarbon calibration tool, 1999, Internet Archaeol., 7, http://intarch.ac.uk/journal/issue7/buckS) based on radiocarbon ages and prior information (i.e., stratigraphical order) as a way to encompass this dilemma. The posterior age depth model presents the radiocarbon ages as the highest posterior density function (HPDF) within the sequence using the Marine09 and a $\Delta R = 200 \pm 200$ to append a marine reservoir effect (Figure 12). It enables significant improvement in terms of precision using HPDF outputs compared with the traditional calibration method of CALIB 6.0. The resulting calibrated ages are consistent with individual ages calibrated with a ΔR close to 400 yrs. This is also consistent with high ΔR previously estimated for the North Atlantic during the last deglaciation [*Bard et al.*, 1994; *Waelbroeck et al.*, 2001; *Bondevik et al.*, 2006; *Cao et al.*, 2007; *Austin et al.*, 2011]. Moreover, a high regional ΔR (>200 yrs) during that period is probably appropriate considering the low ventilation between the ocean and the atmosphere due to (1) the presence of sea ice toward the bay [*de Vernal et al.*, 1987] and (2) meltwater inputs that reduced convection.

4. Results

4.1. Stratigraphy

[15] The photographs and CAT-Scan images (Figures 2, 3, and 12) reveal a highly variable lithology throughout the core. Likewise the grain size distribution shows a broad size range from very fine clay material to coarse sand and up to gravel intervals (Figure 2). Clay content (<2 μm) is relatively stable with values between 20 to 30% except within the 130–170 cm interval where peaks up to 40% and close to 60% are observed. Silt content (2 μm–63 μm) has an average of 45–50% and exhibits a significant increase from 70 cm to the top of the core (60 to >80%). Sandy layers (63 μm–2 mm, Figure 2) are numerous throughout the core with sand percentages of 20 to 30% in distinct intervals and up to 50% between 210–225 cm. Gravel contents (>2 mm) between 10 to 30% occur at very specific depth-intervals. The gravel peaks are associated with sandy layers supporting an ice rafted debris (IRD) transport mode. Between 20 to 100 cm, gravel percent oscillates between 5 and 20%. This is most probably concomitant to the last deglaciation with larger IRD release and meltwater pulses related to the collapse of the large regional ice sheets (IIS, GIS and Baffin Island's ice caps). Grain size sorting (not shown) varies from poorly sorted to very poorly sorted sediment with a trimodal to polymodal mode that demonstrates multiple sediment transport and deposition processes (i.e., hemipelagic, sea-ice, IRD, meltwater pulses, turbidites). Grayish-brown layers (5Y $^5/_2$ - 7.5 YR $^5/_2$) are associated with gravelly sandy mud, higher L* (white) values, high Ca and low Fe and Ti contents (Figure 2). The very top of the core (0–20 cm) is characterized by a brown to dark brown color (10YR $^3/_4$ - 7.5 YR $^4/_2$) illustrated by increasing a* values (red) and a very large increase of the Mn/Ti ratio possibly related to changes in redox conditions (Figure 2) [*Croudace et al.*, 2006], and to increases in Mn-rich sediments that could be synchronous of the Holocene period in the Arctic regions [*Polyak et al.*, 2009]. Mud- to slightly sandy mud layers are dark gray (5Y $^4/_1$) to olive-gray (5Y $^5/_2$), which is reflected by lower L* (black) and a* (green) values coinciding with higher Fe and Ti contents. Pebbles are recognizable on the CAT-Scan images and are most often associated with gravelly sandy mud grayish-brown layers (see lithostratigraphic log on Figures 2, 3, and 12). The density profiles (GRA density and CT number, Figure 2) reveal layers of increased density associated with higher L* values, corresponding to higher Ca and lower Fe contents and lower k_{LF} values. These grayish brown, gravelly to sandy mud decimetric layers (20 to 60 cm) correspond to intervals of higher carbonate content (Figures 2, 3, and 12). These layers are in accordance with the BBDC layers previously reported [*Aksu*, 1981; *Aksu and Piper*, 1987] and summarized by *Andrews et al.* [1998] (see section 2.3).

[16] Based on the core description, physical properties, grain size and previous studies of Baffin Bay marine sediments [e.g., *Aksu and Piper*, 1987; *Andrews et al.*, 1998], we define 4 major sediment

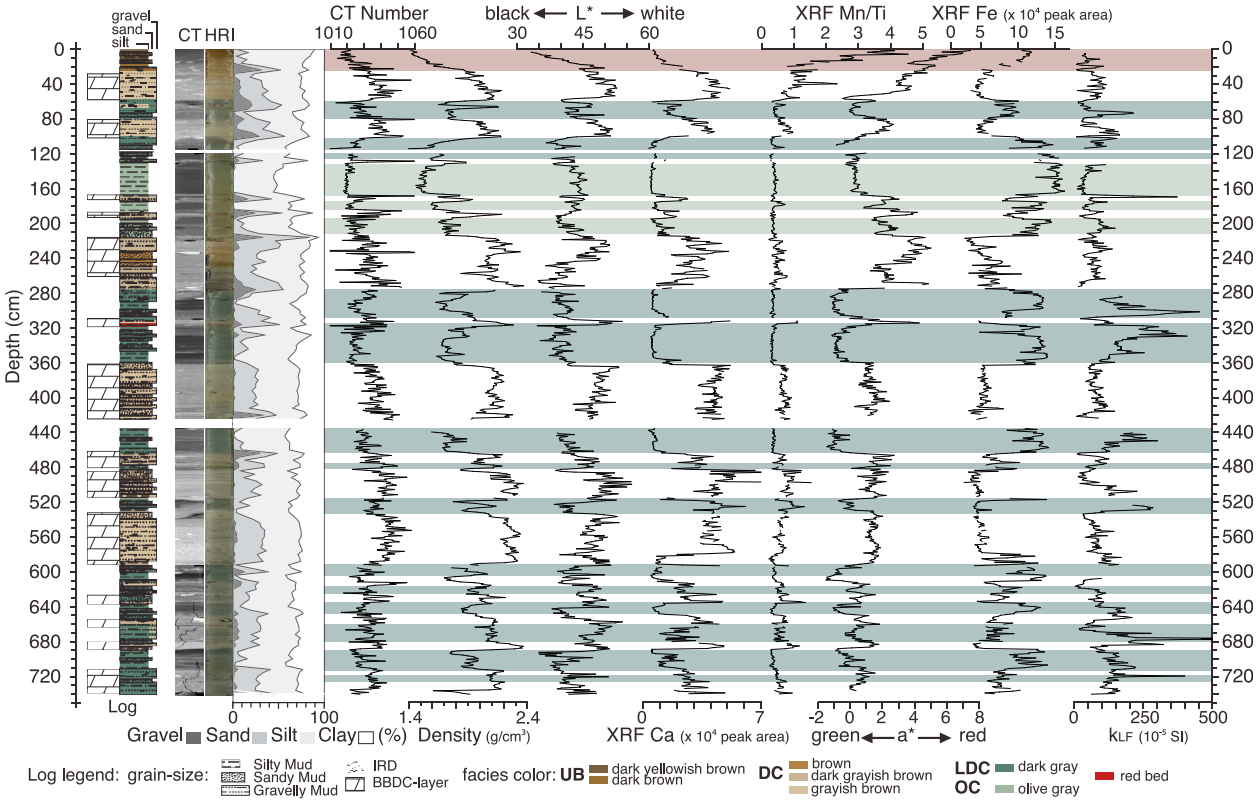

Figure 2. High-resolution physical, geochemical and magnetic properties of core PC16. Log: general simplified stratigraphy of the core (see text and legend for details); CT: CAT-Scan image of the core; HRI: high-resolution digital image; CT Number (density proxy); Density: wet bulk density (gamma-ray attenuation); L*: lightness: black to white; a*: green to red. μXRF peak areas express the relative element concentration of calcium (Ca) and iron (Fe) measured with the ITRAX™ core scanner; Mn/Ti: μXRF element ratio for manganese and titanium. k_{LF}: low-field volumetric magnetic susceptibility. Grain size (%) for clay, silt, sand and gravel measured at 4 cm intervals. Distinct lithological facies are highlighted with color banding. Red: uppermost brownish gray silty mud unit (Uppermost Brownish, "UB"); light green: olive-black silty to clayey mud unit (Olive Clay, "OC"); white: carbonate-rich yellowish-brown to dark-brown very poorly sorted gravelly sandy mud detrital layers (DC); dark green: olive gray to dark gray poorly sorted silty to sandy mud low carbonate detrital layers (LDC) (see text for details).

facies that broadly characterize central Baffin Bay sediments and more precisely core PC16 sediments: (1) Uppermost Brown (UB) – brown to dark brown silty muds; (2) Olive Clay (OC) – brownish-black and olive-black silty muds to clayey muds; (3) Detrital Carbonate (DC) – carbonate-rich yellowish-brown to dark brown very poorly sorted gravelly sandy muds (corresponding to the BBDC-layers); (4) Low Detrital Carbonate (LDC) – olive-gray to dark gray poorly sorted sandy muds to slightly gravelly sandy muds.

4.2. Magnetic Properties

[17] The different lithological facies questions the reliability of a straightforward magnetostratigraphy approach. Accordingly, an extended rock-magnetic description of these lithological facies is needed to assess their magnetic reliability for the recording of a genuine geomagnetic signal.

4.2.1. Magnetic Mineralogy

[18] IRM acquisition curves saturated below 300 mT (Figure 4b), together with the typical shape of hysteresis loops (Figure 4a) suggest that the NRM is carried by low-coercivity magnetic mineral such as magnetite and/or titanomagnetite [*Tauxe et al.*, 1996]. Thermomagnetic analyses (Figure 4c) point out three distinct behaviors during heating: (1) an increase in susceptibility from 200 to 300°C, (2) a weak and continuous loss in susceptibility following the 300°C peak and (3) a significant drop in susceptibility at roughly 580°C (=Curie temperature of magnetite) [*Dunlop and Özdemir*, 2007] in

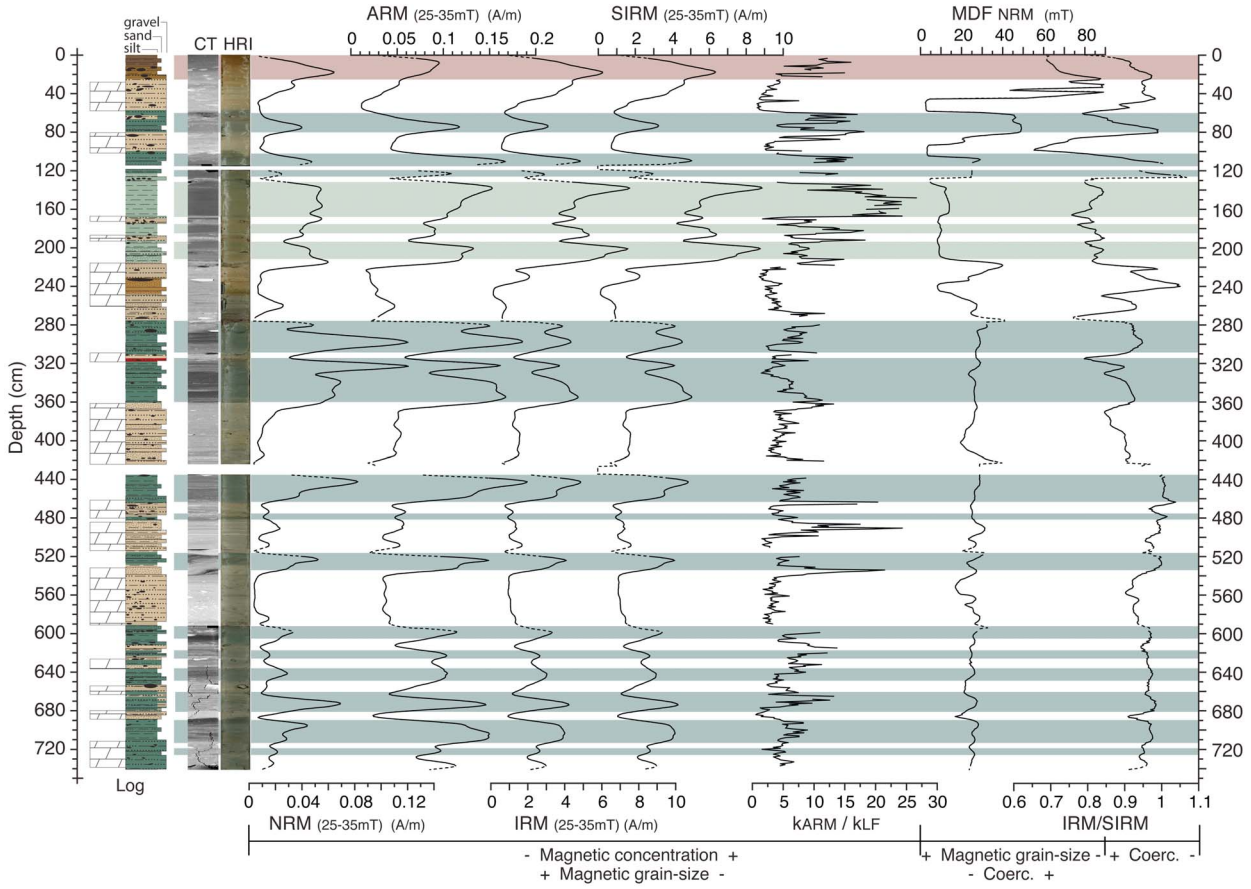

Figure 3. High-resolution magnetic properties of core 16PC. Log: general simplified stratigraphy of the core (see text and legend for details); CT: CAT-Scan images; HRI: high-resolution digital image. Natural (NRM), Anhysteretic (ARM), Isothermal (IRM 0.3 T) and Saturated Isothermal (SIRM 0.95 T) Remanent Magnetization. k_{ARM}/k_{LF}: magnetic grain size indicator. Pseudo-S ratio $IRM_{0.3T}/SIRM_{0.95T}$ calculated after AF demagnetization at peak fields of 25 mT, and MDF_{NRM}: magnetic mineralogy indicator. Distinct lithological facies are highlighted with color banding (see the legend of Figure 2 and text for details).

almost all samples. The drop at the Curie temperature indicates magnetite as the main remanence carrier along the core. The increase in susceptibility during heating together with the higher susceptibility values after the cooling and the asymmetry of the heating and cooling curves are indicative of alteration, transformation and growth of magnetic minerals during the course of the analysis [*Dearing*, 1999; *Maher and Thompson*, 1999]. The decrease in magnetic susceptibility at 300–350°C could be associated with a change of maghemite to hematite [*Dearing*, 1999; *Butler*, 1992], or with some alteration of greigite and/or pyrrhotite [*Maher and Thompson*, 1999] within specific depth-intervals. The presence of greigite is confirmed by gyroremanence (GRM) in the AF demagnetization data of NRM [*Roberts et al.*, 2011] at a few intervals (0–4 cm, 58–88 cm, 102–115 cm, 217–235 cm, 520–535 cm), while pyrrhotite may probably be present within the 130–160 cm depth-interval (olive-black clay sediments, facies "OC") according the values of $SIRM/k_{LF} > 20$ kAm^{-1} (not shown) and $k_{ARM}/k_{LF} > 15$ [*Maher and Thompson*, 1999]. The recovery of the transition temperature near 350°C on the cooling curves (Figure 4c) suggests a Curie temperature for titanomagnetite [*Butler*, 1992]. Within the "Uppermost Brown facies" (upper part of the core), some susceptibility remains after 600°C, hinting at the presence of hematite within the magnetic assemblage at this specific interval which is also characterized by the highest MDF_{NRM} (Figure 3) and a* (red) values (Figure 2). As a whole, the Pseudo-S ratio varies between ~0.8 and 1 (Figure 3). Values higher than 0.9 are observed from the top to 130 cm and from 215 cm to the bottom of the core (except within specific layers, see below), indicating that much of the saturation of the magnetic assemblage is achieved in a 0.3 T field,

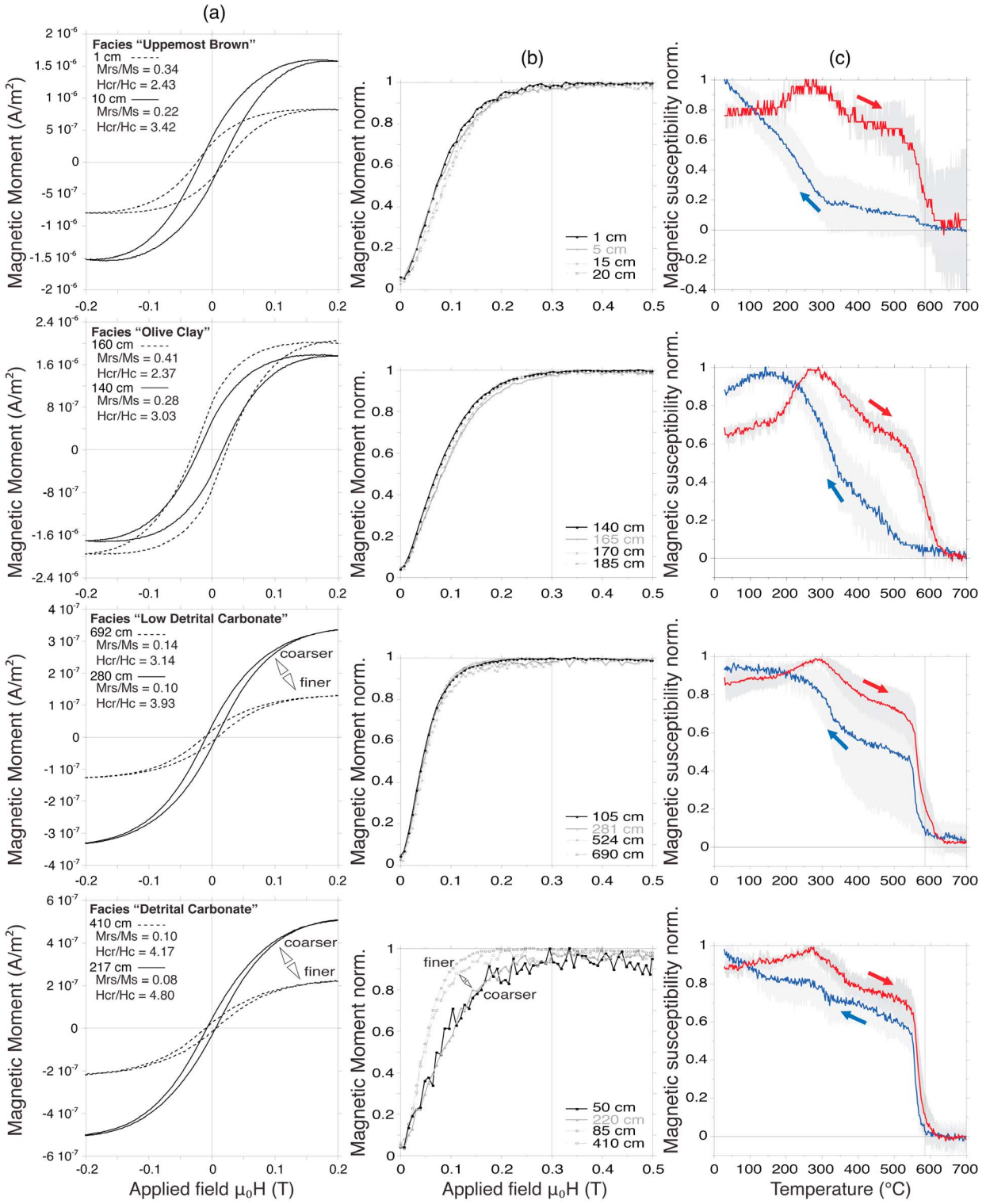

Figure 4. Magnetic mineralogy: (a) Representative hysteresis loops, (b) IRM acquisition curves, and (c) high-temperature dependence of magnetic susceptibility. IRM acquisition and thermal magnetic susceptibility data were normalized. Vertical line at 300 mT is for reference and corresponds to maximal saturation for an assemblage dominated by low coercivity minerals (e.g., magnetite) [*Moskowitz*, 1991]. Vertical line at 580°C corresponds to the Curie temperature of magnetite [*Dunlop and Özdemir*, 1997]. Results are divided in 4 groups according to the 4 facies characterizing the core (see the legend of Figure 2 and text for details).

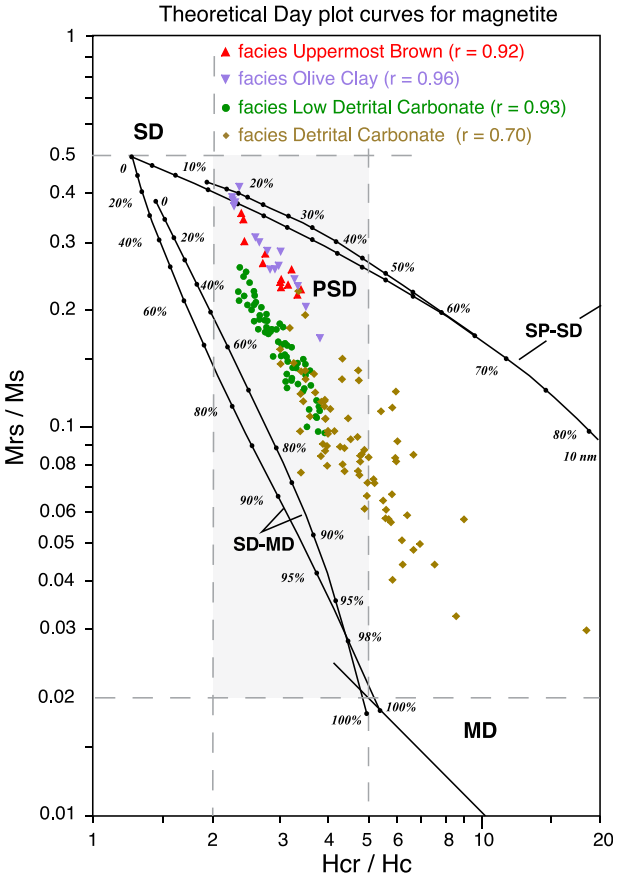

Figure 5. Day plot of selected samples. The horizontal and vertical lines delimitate the theoretical area for single (SD), pseudo-single (PSD) and multi domain (MD) magnetite grains. These lines and the mixing reference curves are from *Dunlop* [2002a, 2002b].

which is consistent with the presence of magnetite and/or titanomagnetite as main remanence. Between 130 and 215 cm, the Pseudo-S ratio shows values close to 0.8 indicating the possible presence of higher coercivity minerals in this interval (i.e., goethite, greigite, pyrrhotite, hematite). MDF_{NRM} values ranging from ~25–30 mT are found from 250 cm to the bottom of the core which again suggests the presence of low coercivity minerals such as magnetite and/or titanomagnetite in this interval [*Dankers*, 1981] (Figure 3). From 80 cm to the top of the core, MDF_{NRM} values sharply increase with values up to 90 mT except very low values (close to 5 mT) within the 45–60 cm and 90–105 cm layers corresponding to larger magnetic grain size (MD grains, Figures 3 and 5) also associated with a gravel peak (Figure 2). These high MDF_{NRM} values could be characteristic of the presence of high-coercivity minerals such as hematite within the mineralogical assemblage. Between 90 to 105 cm, low Pseudo-S ratio values of ~0.7 suggest the apparent presence of higher coercivity minerals such as goethite or hematite. However, when looking at the same ratio but at 0 mT, the values are close to 0.9 (not shown), which are indicative of low coercivity minerals. The difference between the Pseudo-S ratio at 0 and 25 mT thus reflects changes in magnetic grain size and not mineralogy in this specific interval characterized by the presence of gravel. Altogether these results point to magnetite and/or titanomagnetite as being the dominant remanence carriers throughout the core, although iron sulfides, maghemite and hematite may be present within specific depth-intervals.

4.2.2. Magnetic Grain Size and Concentration

[19] Magnetic concentration parameters such as NRM, ARM, IRM, SIRM and k_{LF} (Figure 2 and 3) show increases in the intensity of the remanence and magnetic susceptibility in the Low Detrital Carbonate facies suggesting an increase in the concentration of ferrimagnetic minerals within this facies. Low Detrital Carbonate facies are also characterized by higher k_{ARM}/k_{LF} (Figure 3) values corresponding to finer magnetic grains. The coarsening of magnetic grain size within carbonate layers suggests a distinct origin (or transport process, e.g., IRD) and/or a dilution of the finer ferrimagnetic minerals. Moreover, the lowest k_{ARM}/k_{LF}, NRM, ARM, IRM, SIRM, MDF_{NRM} values indicate the occurrence of somewhat coarser magnetic grain intervals within some specific Detrital Carbonate layers (Figure 3). Such coarse intervals are well illustrated by MD grains within the Day plot (Figure 5). High values of NRM, ARM, IRM, SIRM, k_{ARM}/k_{LF} together with low k_{LF} suggest a relative increase of finer grains (Figures 2 and 3) rather than an overall concentration increase within the "Olive Clay facies." This is also illustrated by a close match between the clay percent and k_{ARM}/k_{LF}, which supports the presence of finer magnetic grains throughout the Olive Clay facies. In addition, higher Mrs/Ms values (0.35–0.4) and wider hysteresis loops (Figure 4a) are found within the Olive Clay facies and are indicative of finer grains (PSD to SD domain; Figure 5), whereas Mrs/Ms values ranging between 0.1 and 0.3 characterize the bulk of the core and are typical of relatively coarser PSD titanomagnetite grains [*Day et al.*, 1977; *Tauxe*, 1993; *Dunlop*, 2002a] (Figure 5). Sediments from the Uppermost Brown, Olive Clay and Low Detrital Carbonate facies are well distributed ($r > 0.92$) along mixing lines within the PSD domain (1–15 μm; Figure 5), while some Detrital Carbonate layers are found in the MD domain

according to the Day plot [*Day et al.*, 1977; *Dunlop*, 2002a]. DC-layers are also characterized by a more heterogeneous magnetic grain size distribution (r = 0.7). Uppermost Brown and Olive Clay facies' grains are slightly shifted upward toward the SD domain (also revealed by the hysteresis shape, Figure 4a) indicating finer ferrimagnetic grains.

[20] In summary, the sedimentary sequence is composed of 4 distinct magnetic assemblages: (1) low coercivity ferrimagnetic minerals within the PSD range, which characterize a "background" facies corresponding to the Low Detrital Carbonate facies; (2) finer magnetic minerals within the SD – PSD range characterizing the Uppermost Brown (upper 20 cm) and Olive Clay (130–215 cm) facies, possibly containing a fraction of higher coercivity minerals; (3) low coercivity ferrimagnetic minerals in the coarse PSD range with lower magnetic concentration, characterizing the main fraction of the Detrital Carbonate layers; and (4) low coercivity ferrimagnetic minerals in the MD domain associated with magnetic dilution and coarse grains.

4.3. Natural Remanent Magnetization

[21] The vector end-point diagrams [*Zijderveld*, 1967] reveal the presence of two magnetic components that characterize the magnetic recording (Figure 6): a very low coercivity component (viscous magnetization) easily removed after a AF demagnetization between 5–15 mT, and a stable well-defined characteristic remanent magnetization (ChRM). The maximum angular deviation (MAD) values are lower than 5° for most of the core (87.5% of the whole core, Figure 7a), which is considered as excellent quality data [*Stoner and St-Onge*, 2007]. MAD values between 8 and 12°, which are still considered as good quality data [*Butler*, 1992; *Opdyke and Channell*, 1996], are only found in very few Detrital Carbonate layers (2.3% of the total measurements) characterized by MD magnetic grain and/or edges of the u-channels (Figure 5 and 7a) while the remaining MAD values are found between 5 to 8°. As a whole, the Characteristic remanent magnetization (ChRM) inclinations (Figure 7b) fluctuate around the expected inclination based on a geocentric axial dipole (GAD) model for the latitude of the coring site (I_{GAD} = 79.9°), indicating a well-preserved and high-quality paleomagnetic signal [e.g., *Stoner and St-Onge*, 2007].

[22] To summarize all magnetic data, most of the sedimentary sequence is characterized by a well-defined and strong ChRM carried by low coercivity minerals within the PSD range and following a magnetite mixing line. Nonetheless, the presence of secondary magnetic minerals such as iron sulfides, hematite and/or maghemite may be found in specific intervals, but these intervals represents only ~16% of the core and are not associated with key intervals such as the RPI peaks and troughs used for the establishment of the age-model (see below). In addition, several thin layers corresponding to the sandiest intervals (Figures 2 and 8) are identified by a larger grain size in the MD domain (Figures 3 and 5) and will have to be taken with caution (especially when corresponding to MAD > 5°, Figure 7) for relative paleointensity (RPI) reconstruction. Concentration and grain size variability remain below a factor 10 (reliable for RPI study) if such specific DC layers are excluded (gray shaded areas on Figures 7 and 8). Nonetheless, as noted by *Stoner et al.* [2000], thin sand layers (with MD grains) within a sediment sequence could still be suitable for paleomagnetic studies as they may not significantly influence the rock magnetic properties of the remanence carriers. Moreover, *Spassov and Valet* [2012] demonstrated that the depositional remanent magnetization (DRM) of carbonate-rich sediments is linearly related to the field intensity, confirming their reliability for RPI studies. Their experiments also suggest that down-core changes in carbonate content do not affect the response of the magnetization to the field.

4.4. Relative Paleointensity (RPI) Determination

[23] Estimation of the relative paleointensity (RPI) of the geomagnetic field in sedimentary sequences is a function of the natural remanent magnetization carried by the detrital ferrimagnetic grains (see *Tauxe* [1993], *Tauxe and Yamazaki* [2007] and *Valet* [2003] for extended reviews). However, the intensity of the remanence is also influenced by changes in the magnetic mineralogy, concentration and grain size. Thus the NRM must be normalized by an appropriate magnetic parameter in order to compensate for these "non-geomagnetic field" imprints. Concentration dependent parameters such as laboratory-induced magnetizations (ARM, IRM and SIRM) or k_{LF} are commonly employed as normalizers in literature [e.g., *King et al.*, 1983; *Tauxe*, 1993; *Tauxe and Yamazaki*, 2007].

[24] To validate the reliability of the RPI proxy, several criteria must be satisfied:

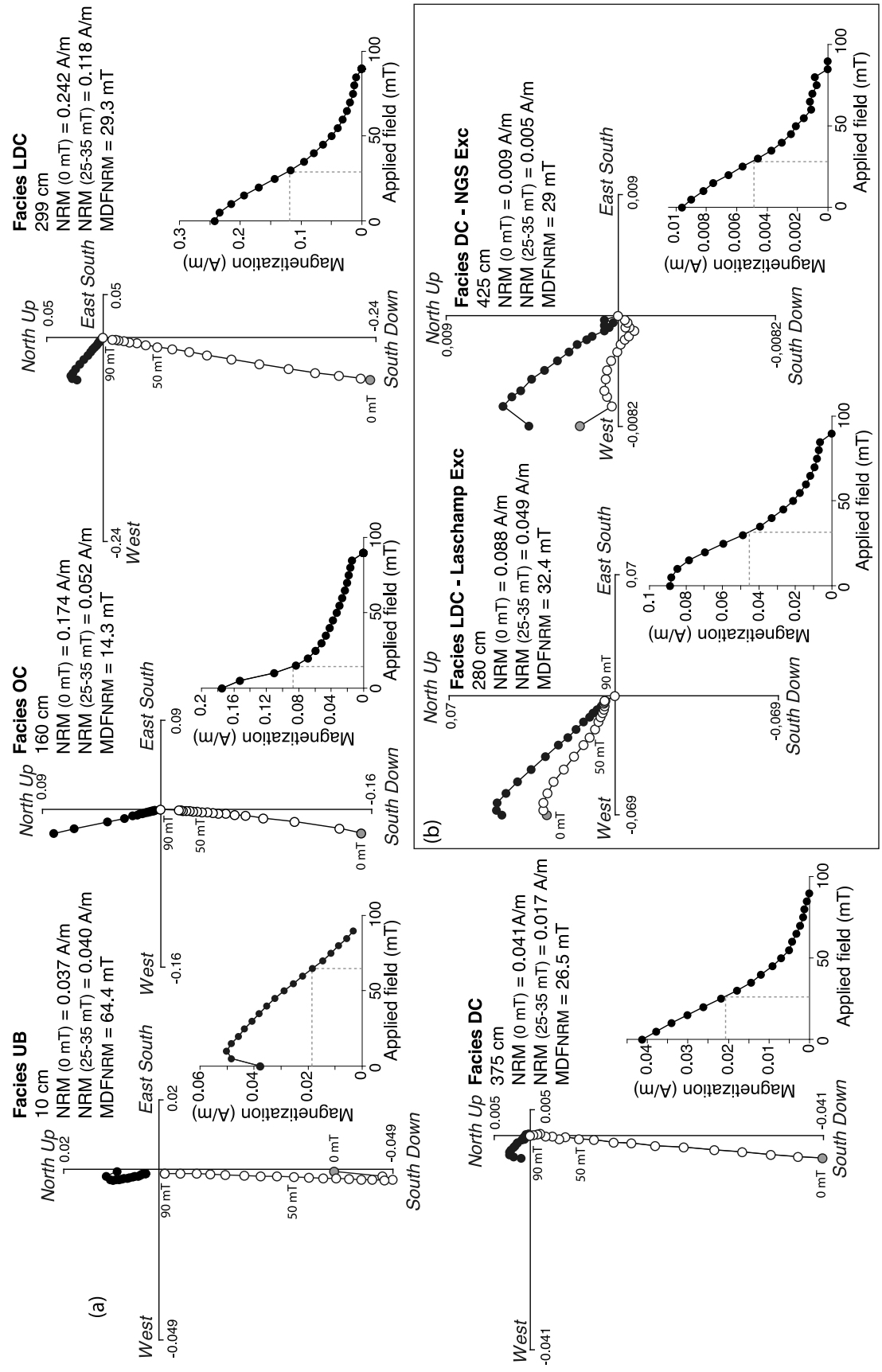

Figure 6. Paleomagnetic vectors. (a) Typical representative vector end-point orthogonal projection diagrams and AF demagnetization diagrams for the 4 facies discussed in the text. Open (closed) circles indicate projections on the vertical (horizontal) plane. (b) Typical vector end-point projection diagrams and AF demagnetization diagrams at the two intervals where geomagnetic excursions were identified (see also Figure 7).

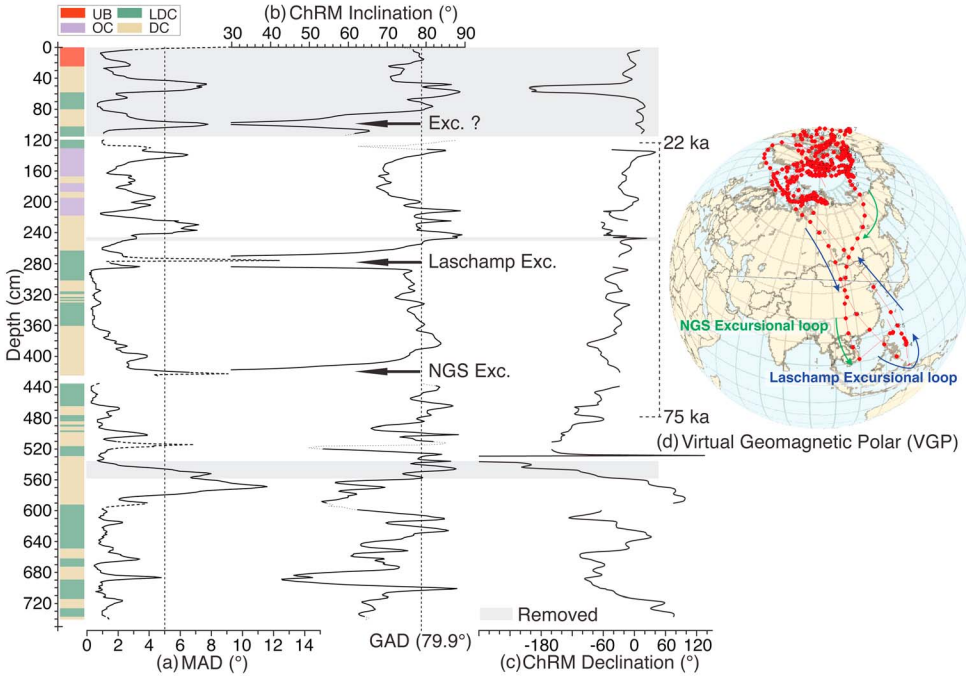

Figure 7. Characteristic remanent magnetization (ChRM). (a) MAD (Maximum Angular Deviation) values, (b) Inclination and (c) Declination. The solid vertical line indicates a MAD value of 5°, whereas the broken vertical line in the ChRM inclination represents the expected inclination for a geocentric axial dipole model (I_{GAD} = 79.9°). Gray shaded areas indicate problematic intervals for paleomagnetic reconstruction (see text for details). Data near core breaks are represented as a dotted line. Two potential geomagnetic excursions have been identified: the Laschamp (41 ± 1 ka) [*Lund et al.*, 2006] and the Norwegian-Greenland Sea (61 ± 2 ka) [*Lund et al.*, 2006] excursions. (d) Virtual Geomagnetic Pole (VGP) calculated within the 22–75 cal ka BP time interval. The facies are represented on the left side with distinct colors: uppermost brown (red), olive clay (purple), low detrital carbonate layers (green) and detrital carbonate layers (beige) (see text for details).

[25] 1. The NRM must be characterized by a strong, stable and single component magnetization carried by low coercivity ferromagnetic grains (e.g., magnetite) within the SD – PSD range [*King et al.*, 1983; *Tauxe*, 1993]. Moreover, changes in the magnetic concentration should not vary by more than a factor 10 [*Tauxe*, 1993]. As discussed earlier, with the exception of some specific intervals (not used for RPI determination), the magnetic mineralogy for the bulk of the core is well-suited for paleointensity determination with the presence of magnetite in the PSD grain size range with a strong, stable and well-defined ChRM (Figures 4, 5, and 6).

[26] 2. The normalizer should activate the same grains that carried the NRM [*Levi and Banerjee*, 1976]. k_{LF} being sensitive to large MD magnetite grains as well as superparamagnetic (SP) grains, which do not carry a magnetic remanence, it was considered as an inappropriate normalizer in this environment heavily impacted with coarse ice rafted debris layers. In addition, the presence of coherency (high values of the Blackman-Tuckey cross-spectral analysis using a Bartlett window at 95% confidence level), and a linear correlation coefficient of −0.33 between NRM/k_{LF} and k_{LF} (auxiliary material Figure S2a) reveal an incomplete normalization or an over correction [*Tauxe and Yamazaki*, 2007].[1] The next possible normalizers are the ARM and IRM. The ARM is often chosen as a normalizer because it activates PSD grains of magnetite, whereas IRM can also activate a large fraction of magnetic grains (MD) that do not carry the NRM [*Levi and Banerjee*, 1976]. To select the demagnetization interval and normalizer that best mimics the coercivity spectrum of the NRM, we compared the slope of the NRM, ARM and IRM intensity from several demagnetization steps [*Levi and Banerjee*, 1976]. Linear correlation coefficients (r) were calculated in order to quantify the relationship throughout the whole core [*Channell et al.*, 2002]: r-value close to 1 being indicative of well-defined slopes with coercivity of

[1]Auxiliary materials are available in the HTML. doi:10.1029/2012GC004272.

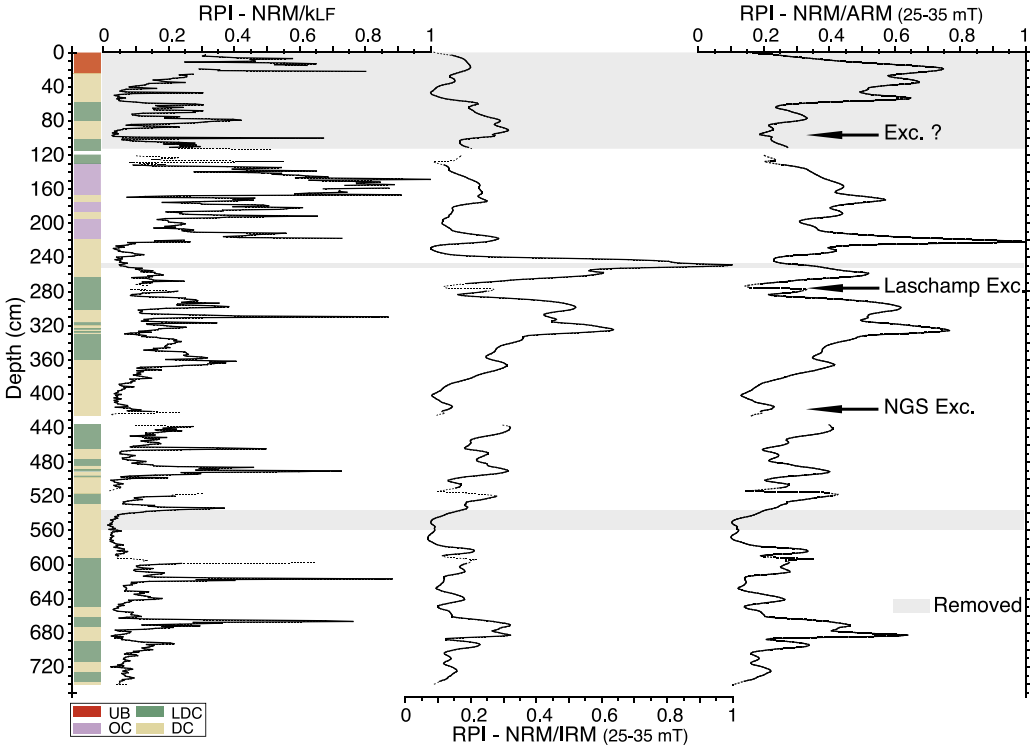

Figure 8. Normalized relative paleointensity. (left) NRM/k_{LF}, (middle) NRM/IRM (25–35 mT), (right) NRM/ARM (25–35 mT). Two potential geomagnetic excursions (see also Figure 7) characterized by low intensities are illustrated: the Laschamp (41 ± 1 ka) [*Lund et al.*, 2006] and the Norwegian-Greenland Sea (61 ± 2 ka) [*Lund et al.*, 2006] excursions. The facies are represented on the left side with distinct color: uppermost brown (red), olive clay (purple), low detrital carbonate layers (green) and detrital carbonate layers (beige) (see text for details). Data near core breaks are represented as a dotted line.

the normalizer that activates the same coercivity than the NRM. The best r-values were found for the 25–35 mT AF demagnetization interval (auxiliary material Figure S1) for both ARM and IRM. The r calculated against ARM present very few values <0.99, while correlations with IRM show r < 0.95 for some specific intervals (45–60 cm, 95–105 cm, 245–250 cm and 535–560 cm) corresponding to intervals of low MDF_{NRM}, high MAD values and/or presence of secondary magnetic minerals such as greigite or maghemite. Within these intervals, and more largely for the whole core, the ARM coercivity spectra seem to best mimic the NRM than the IRM ones.

[27] 3. The RPI proxy cannot be correlated with its normalizer or with any lithological proxy [*Tauxe and Wu*, 1990]. Here, the relative paleointensity estimates (RPI) do not correlate with their normalizer (r < 0.2) (auxiliary material Figure S2a). Furthermore, we tested the coherence between both RPI estimates and their respective normalizers using a Blackman-Tuckey cross-spectral analysis with a Bartlett window at 95% confidence level [*Paillard et al.*, 1996]. The cross-spectral analysis reveals that the RPI proxies are not coherent with their normalizers for the majority of the core but present some coherency over few specific intervals (auxiliary material Figure S2a). We also tested the coherence of NRM/ARM and NRM/IRM with lithological proxies such as MDF_{NRM}, k_{ARM}/k_{LF} and IRM/SIRM (auxiliary material Figures S2b and S2c). NRM/IRM is not coherent nor correlated with these proxies (r < 0.1), while NRM/ARM is slightly more coherent with NRM_{MDF} (r = 0.28). When comparing both NRM/ARM and NRM/IRM proxies (Figure 8), the same variability is observed from 120 cm to the bottom of the core, while RPI estimates present distinct features from 115 cm to the top of the core. When removing the section 0–115 cm, NRM/ARM presents no coherency or correlation (r = 0.05) with NRM_{MDF}. The clear mismatch between both RPI curves and the extreme MDF_{NRM} and IRM/SIRM fluctuations at the top of the core (0–115 cm) lead to a doubtful recording of the genuine geomagnetic field in that specific interval.

[28] Based on these results, we selected the $ARM_{25–35\ mT}$ as the best normalizer. It activates the same magnetic assemblages than the $NRM_{25–35mT}$ and presents no correlation with lithological proxies. However, some problematic layers will have to be treated with caution or removed from the record as their coarser (e.g., $MDF_{NRM} < 5$) magnetic grains may have diminished the effectiveness of the normalization (shaded area in Figures 7, 8, and 9).

5. Discussion

5.1. Age/Depth Relationship

[29] In order to establish an original age-depth relationship in central Baffin Bay, an environment characterized by significant calcium carbonate dissolution and the problematic use of ^{18}O stratigraphies (see sections 1 and 2.1), we compared the core PC16 RPI record with several well-dated RPI records and stacks (Figure 9). Nonetheless, the establishment of an age-depth relationship for the top of the core based on RPI correlations still presented some difficulties due to the lower quality of the remanence carrier that characterizes the interval 0–115 cm (see sections 4.2 and 4.4). Therefore, in order to propose an original age model for that period we correlated the relative percentages of calcite between the PC16 record and a nearby well-dated box core from Baffin Bay (core JCR175-BC06) studied by *Andrews and Eberl* [2011] (Figure 11). The records from BC06 and PC16 were correlated (r = 0.975) with 10 tie points using the AnalySeries program [*Paillard et al.*, 1996]. It enables to transfer the chronology of core BC06 to core PC16 (Figure 11). The robust correlation between both mineralogical signals together with the good fit between the interpolated age model and the 3 available radiocarbon ages allow a pretty strong chronology for that problematic interval even if it is set from an indirect approach (changes in sediment mineralogy).

[30] Between 125 and 478 cm, the age model was established by correlating core PC16 to the North Atlantic relative paleointensity stack (NAPIS-75) [*Laj et al.*, 2000] (between 22 to 75 ka) with 21 tie points (peaks and troughs, Figure 9 and Table 2) using the AnalySeries program. The best correlation coefficient (r = 0.8) was obtained by sliding the two curves with respect to each other (Figure 10). The incertitude in the age model for the 22–75 ka interval corresponds to the $\pm 2\sigma$ incertitude from the NAPIS bootstrap calculation (gray area on Figures 9, 10, and 12). The use of the NAPIS-75 stack, that compiled 6 North Atlantic marine cores spanning the last 10–75 ka [*Laj et al.*, 2000], as the main reference is particularly interesting because (1) the stacking process has removed the variability induced by the lithology or regional magnetic origins (i.e., non-dipole field), (2) post-depositional magnetization acquisition are considered negligible in the NAPIS-75 stack [*Kissel et al.*, 1999; *Laj et al.*, 2000], and (3) the NAPIS-75 age model was correlated at the millennial scale and placed on the GISP2 age scale, allowing a robust chronology. The RPI record from 480 to 741 cm was correlated using 14 tie-points with 6 well-dated individual records and stacks (Figure 9). The individual RPI reference curves are from (1) the Labrador Sea: cores MD95–2024 [*Stoner et al.*, 2000] and 094PC [*Stoner et al.*, 1996, 1998] and (2) the North Atlantic: ODP site 983 [*Channell et al.*, 1997]. The RPI marine stacks include (1) the high-resolution Mediterranean and Somali region stack [*Meynadier et al.*, 1992] and (2) the low resolution Sint200 [*Guyodo and Valet*, 1996] and PISO-1500 [*Channell et al.*, 2009] stacks, from Atlantic, Mediterranean, Indian and western Pacific records. The temporal shifts observed between these records are represented by the standard deviation between the 6 references curves (gray area on Figure 12) and are due to their intrinsic chronological uncertainties. The different sedimentation rates and lock-in depths of the distinct records could explain part of the differences observed in the amplitude of relative paleointensity variations. Also, some non-dipole component (especially where very high sedimentation rates were recorded) could be part of individual records, possibly accounting for some relative differences between paleointensity features.

[31] The RPI record of core PC16 is remarkably in agreement and present strong coherency (at 95% confidence level using Blackman-Tuckey cross-spectral analysis with a Bartlett window) with the NAPIS-75 stack (Figure 10 and auxiliary material Figure S3). Similarly, the relatively strong correlation coefficients obtained between core PC16 and several other individual high-resolution RPI records and stacks further supports the geomagnetic origin of the signal (Figure 9) in the 20–75 ka interval (Figure 9). Between 75 and 100 ka (where each data set overlap), the overall agreement between the main RPI features in PC16 and other reference curves (Figure 9) also supports the age-model established. However, the correlation coefficients calculated in this interval present lower values, which can be explained by (1) low-resolution stacks (i.e., Sint200, PISO-1500) with low

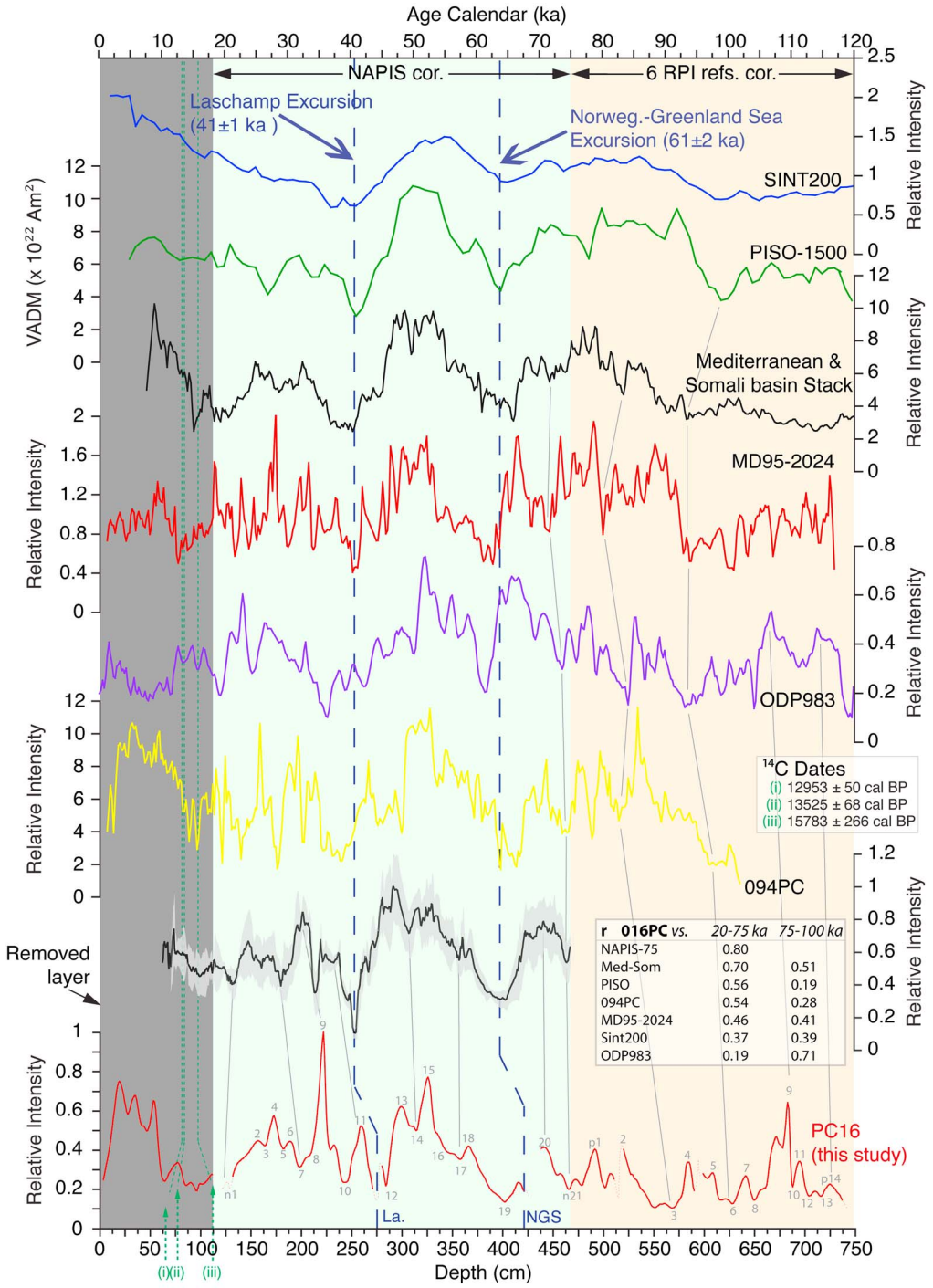

Figure 9. RPI correlation. Relative paleointensity inter-comparison between core PC16 (this study) and RPI reference curves from the Labrador Sea: cores MD95-2024 [*Stoner et al.*, 2000] and 094PC [*Stoner et al.*, 1996, 1998]; the North Atlantic: ODP983 [*Channell et al.*, 1997]; NAPIS-75 (stack of six RPI records from the North Atlantic Ocean) [*Laj et al.*, 2000]; Mediterranean and Somali Stack [Meynadier *et al.*, 1992]; and global stacks: Sint200 [*Guyodo and Valet*, 1996], and PISO-1500 [*Channell et al.*, 2009]. The 22–75 ka interval was dated by correlation with the NAPIS-75 stack solely, while the 75–115 ka interval was dated using 6 reference curves. The correlation coefficients were calculated between each data set within the 20–75 and 75–100 ka intervals in order to provide statistical information where all the records overlap (see text for details).

Table 2. Age Model and Tie-Points

Depth PC16 (cm)	Age[a] (cal ka BP)	Error[b]	Tie-Points[c]
0	0		C1
16.5	10		C2
20	10.7		C3
24	10.8		C4
32	11		C5
40	11.4		C6
48	11.9		C7
56	12		C8
60	12.2		C9
64	12.8		C10
125	21.4	0.98	N1
157	24	1.19	N2
164	24.5	1.54	N3
174	25	1.74	N4
183	26	1.21	N5
190	27	1.06	N6
198	29	2.15	N7
208	31.5	0.64	N8
223	32.5	2.2	N9
246	34.5	1.27	N10
260	36.5	1.46	N11
275	**40.7**	**1.55**	**Laschamp**
284.5	43	1.1	N12
300	47	1.7	N13
315	49.5	1.46	N14
326	52.5	1.3	N15
346	56	1	N16
358	57.5	1.19	N17
367	59	0.83	N18
403	62.5	1.27	N19
422	**64.5**	**1.65**	**NGS**
441	71	1.92	N20
478	74	1.07	N21
492	76.8	1.94	P1
520	80.1	1.24	P2
568	82.7	2.35	P3
584	84.9	2.39	P4
608	90.5	2.81	P5
628	94.7	3.03	P6
641	97	3.05	P7
651	99.2	0.96	P8
684	104	2.39	P9
688	104.9	2.29	P10
695	107	2	P11
704	108.9	2.45	P12
715	110.5	2.48	P13
725	112.4	1.56	P14

[a]Tie-points age for: calcite correlation, NAPIS correlation and correlation based on the 6 references curves (see text for details). The excursions are in bold.

[b]Time incertitude: for 22–75 ka interval, it corresponds to the $\pm 2\sigma$ incertitude from the NAPIS bootstrap calculation. For the 75–115 ka interval, the errors correspond to the standard deviation between the 6 references curves.

[c]Tie-points: C = calcite; N1–N21 = NAPIS; P1–P14 = 6 reference cores.

variability, (2) highly variable sedimentation rates between cores (for instance, the best correlation (r = 0.71) is calculated with core ODP983, which have similar sedimentation rates with PC16 in this time period, i.e., ~10 cm/ka) [*Channell et al.*, 1997] and (3) uncertainty of the respective age models based on low-resolution isotopic stratigraphies [*Stoner et al.*, 1996, 1998, 2000; *Guyodo and Valet*, 1996].

5.2. Paleomagnetic Secular Variations and Excursions in Baffin Bay

[32] Two large declination changes are observed at 2 intervals that have been excluded based on rock-magnetism analyses (Figure 7c). The first one (46–62 cm) is located within a coarse sediment interval (MDF_{NRM} < 5 and MD grain, Figures 3 and 5), while the second one is a remobilized facies (525–545 cm, CT image). It demonstrates the lithological influence on the declination in these specific intervals (note that these intervals have been removed for the RPI reconstruction, see sections 4.2 and 4.4). While the inclination record generally oscillates around the expected GAD values, 3 inclination lows (Figure 7b) present large deviations from the GAD (>40°) and are associated to low geomagnetic intensity (95–105 cm; 270–290 cm; 415 cm – section break). Such a pattern is commonly considered as a geomagnetic excursion [*Laj and Channell*, 2007]. The 95–105 cm (~14.8–15.5 cal ka BP) large deviation is recorded within a layer characterized by coarse magnetic grains (with MDF_{NRM} < 5 and MD grain) and the paleomagnetic results are most likely attributed to lithological overprints. The 2 remaining large deviations are found in sedimentary layers that may be seen as reliable recorders of the genuine state of the geomagnetic field. Unfortunately, these potential excursions are located near section breaks and are characterized by 8 and 6 data points, respectively (excluding the deleted data at section break), hence questioning their magnetic origin. Yet the paths of the Virtual Geomagnetic Poles (VGPs, Figure 7d) toward the Southern Hemisphere during these 2 intervals are relatively similar to the ones observed for the Norwegian-Greenland Sea and Laschamp geomagnetic excursions except for the sense of looping [*Laj and Channell*, 2007; *Laj et al.*, 2006; *Lund et al.*, 2005]. The details of the field behavior (i.e., sense of looping and paths) during these excursions could have been poorly recovered considering the low sedimentation rates (<8 cm/ka) and the smoothing associated with post-depositional remanent magnetization acquisition [*Roberts*, 2008]. It might explain the discrepancy with the above references. These two large inclination lows are recorded at ca. 40.9 and 64.8 cal ka BP (respectively) according to the constructed age

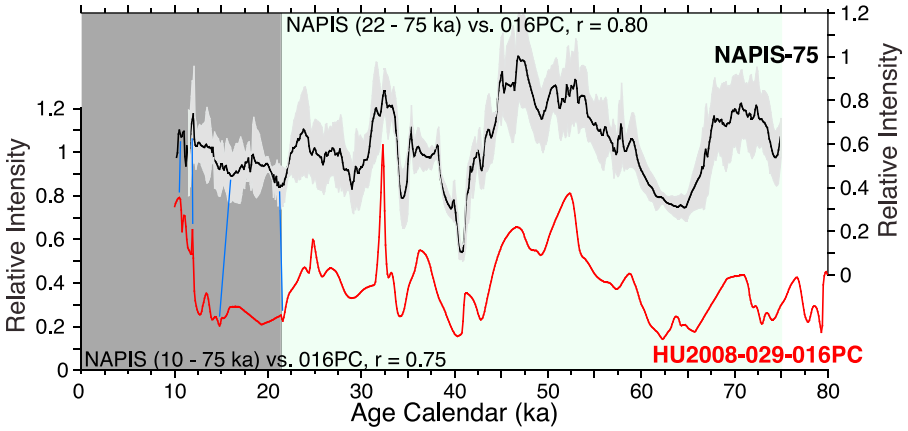

Figure 10. Relative paleointensity correlation between core PC16 and the NAPIS-75 stack (stack of six RPI records from the North Atlantic Ocean) [*Laj et al.*, 2000]. Blue lines represent similar features in both RPI records (not used for the age/depth relationship establishment).

model. The timing is thus consistent with the Laschamp (41 ± 1 ka) [*Lund et al.*, 2006] and the Norwegian-Greenland Sea (61 ± 2 ka) [*Lund et al.*, 2006] excursions, which in turn supports their excursional origin. However, several low inclinations in sedimentary cores from the Arctic have been recently attributed to partially self-reversed CRM carried by titanomaghemite and acquired during the oxidation of detrital (titano)magnetite grains rather than representing genuine geomagnetic excursions [*Channell and Xuan*, 2009; *Xuan and Channell*, 2010; *Xuan et al.*, 2012]. Since oceanographic conditions in Baffin Bay are broadly similar to the Arctic Ocean and since no NRM thermal demagnetization experiments were carried out in this study, a partially self-reversed CRM carried by titanomaghemite cannot be excluded and could explain the low inclination values in Baffin Bay rather than representing real excursions. However, the correspondence and timing of the two excursions in core PC16 with previously published records together with the contemporaneous RPI lows support a geomagnetic origin.

[33] Several excursions have already been observed in numerous Baffin Bay cores but previous age models based on lithological inter-core correlations did not permit a clear identification of these events [*Aksu*, 1983b; *Thouveny*, 1988]. *Thouveny* [1988] identified two potential excursions dated around 18 and 24 cal ka BP (at ~0.9 and 2.5 m respectively) within a piston core (HU85-027-016PC) collected at ODP site 645. The large inclination deviation recognized in core PC16 between 95–105 cm (~14.8–15.5 cal ka BP) could possibly be related to the low inclination dated at 18 cal ka BP in core HU85-027-016PC considering uncertainties in the corresponding age model based on 2 radiocarbon ages and an open discussion on the oxygen isotopic stratigraphy. However, the corresponding pattern in PC16 is believed to be of lithological origin (Figure 7), which therefore questions the excursional nature of the inclination low in core HU85-027-016PC. We propose to relate this inclination low to a lithological imprint rather than representing an excursion as previously proposed [*Thouveny*, 1988]. The second large inclination deviation occurred at 2.5 mbsf (~24 cal ka BP) in core HU85-027-016PC. We do not observe any deviation of the inclination at this depth in core PC16 but according to the geographical proximity of these 2 cores (same site), and assuming the same sedimentation deposition regime, it is coeval with an intensity low recorded at 246 cm in core PC16 and dated at 34.5 ± 0.35 ka (tie-point: N10, Figure 9). We propose to adjust the age of the excursion observed in core HU85-027-016PC from 24 cal ka BP to ca. 34.5 cal ka BP to be synchronous with the Mono Lake excursion [*Lund et al.*, 2006]. According to our results, we believe that previous deep central Baffin Bay chronological frameworks [*Aksu* 1981, 1983a; *Aksu and Piper*, 1979, 1987; *de Vernal et al.*, 1987; *Thouveny*, 1988; *Hillaire-Marcel et al.*, 1989] were problematic due to the (1) scarcity of ^{14}C ages together with inaccurate $\delta^{18}O$ interpretations [*Hillaire-Marcel and de Vernal*, 2008], and (2) false assumption of nearly constant sedimentation rates, all leading to an incorrect identification of geomagnetic excursions. We therefore propose to relate the excursions

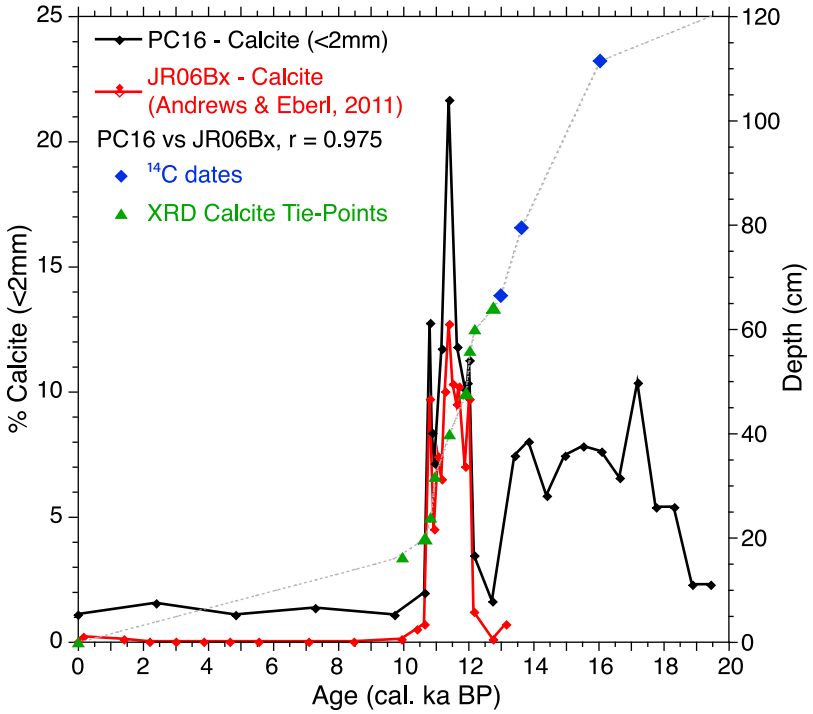

Figure 11. Age/depth relationship for the top of the core. Correlation between calcite percentages between JCR175BC06 box core (wt. %) [*Andrews and Eberl*, 2011] and PC16 (left axis). Calcite-derived tie points (green triangle) and radiocarbon dates (blue diamonds) are plotted against depth (right axis). The correlation (r = 0.975) and radiocarbon dates enable to propose an original age/depth relationship where rock magnetic results are not suitable for paleomagnetic correlation.

described by *Aksu* [1983b] in several cores collected in the 1970s (between 250 and 450 cmbsf) to the Mono Lake or the Laschamp events (33 ± 1 cal ka BP or 41 ± 1 ka cal BP) [*Lund et al.*, 2006] rather than the Blake event (123 ± 3 cal ka BP) [*Lund et al.*, 2006]. Our findings here clearly rules out the low sedimentation rate model for Baffin Bay. As a general comment, this confirms the extreme caution to be taken before interpreting excursions in Arctic or sub-Arctic sediments [*St-Onge and Stoner*, 2011] because of (1) uncertain chronologies and (2) lithological or diagenetic effects [*Channell and Xuan*, 2009; *Xuan et al.*, 2012].

5.3. Chronostratigraphy in Central Baffin Bay

[34] The RPI correlations along with the recognition of two possible excursions strongly support the proposed chronostratigraphy for the last climatic cycle (~0–115 ka). The derived age-model (Figure 12) yields a mean sedimentation rate of ~6.5 cm/ka. This is slightly lower that the high sedimentation rate hypothesis estimated from previous studies of central Baffin Bay sediments (8–12 cm/ka) [*de Vernal et al.*, 1987; *Andrews et al.*, 1998] but still coherent considering (1) previous age models confidence, and (2) uncertainty on precise BBDC duration in the core. The low sedimentation rates in Baffin Bay reflect an overall dry-base character of ice sheets in source areas [*Aksu*, 1981; *Andrews et al.*, 1985; *Aksu and Piper*, 1987; *Hiscott et al.*, 1989; *Hillaire-Marcel et al.*, 1989]. According to the proposed age model, the sedimentation rates varied largely from values <5 cm/ka to 20 cm/ka, and up to 35 cm/ka immediately after the Younger Dryas (Figure 12). While the "background" facies corresponds to lower sedimentation rates (3 to 6 cm/ka), the inter-bedded layers depict three to four fold higher rates. The 3 AMS ^{14}C dates support the higher sedimentation rates during the last Termination (Table 1 and Figures 11 and 12). This nonlinear sedimentation pattern is not surprising due to: (1) facies variability throughout the core; and (2) the core location within the confined Baffin Bay's sedimentary basin associated with a highly variable depositional environment (e.g., rapidly deposited layers)

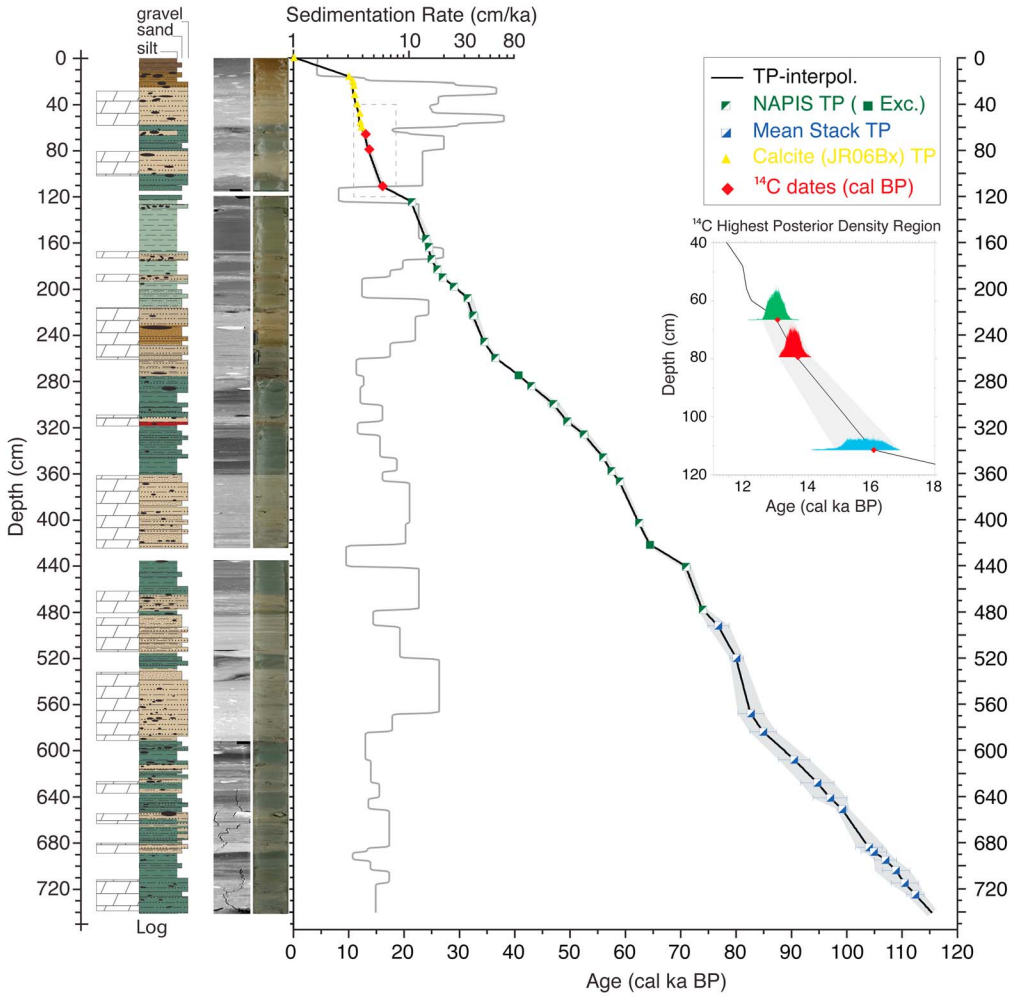

Figure 12. Age/depth relationship and associated sedimentation rates for core PC16. The age model is based on the RPI comparison (Figure 9). NAPIS related tie-points (TP) are represented by green squares. Tie-points derived from the 6 reference curves are illustrated by blue squares. Three radiocarbon ages (red diamonds) and 2 potential geomagnetic excursions (green filled square) at 41 ± 1 ka and 61 ± 2 ka support the chronology. The radiocarbon ages are presented as the highest posterior density function within the sequence using the Marine09 and a $\Delta R = 200 \pm 200$ to append the marine reservoir effect. Incertitude in the age model is represented by shaded area. For the 22–75 ka interval, it corresponds to the $\pm 2\sigma$ incertitude from the NAPIS bootstrap calculation. For the 75–115 ka interval, the errors correspond to the standard deviation between the 6 references curves.

correlated with last glacial cycle short events (e.g., ice surges).

6. Conclusions

[35] This high-resolution rock-magnetic and paleomagnetic analysis of a central Baffin Bay sedimentary sequence spanning the last climatic cycle indicates that the magnetic remanence is mainly carried by magnetite in the PSD range throughout most of the core. A strong relationship between lithological facies and magnetic signatures prevails. Detrital carbonate layers (BBDC) are characterized by coarse magnetic grain size (coarse PSD to MD domain) and a low ferrimagnetic concentration. Holocene and last glacial maximum (LGM) sediments contain fine magnetic grains (PSD to SD domain) and have a high ferrimagnetic concentration. Despite the identification of several sedimentary facies and high lithological variability, we were nonetheless able to derive a reliable RPI proxy for much of the core. The directional data also allowed the recognition of two geomagnetic excursions, the Laschamp and Norwegian-Greenland-Sea excursions. The relative paleointensity correlations with well-dated RPI records and stacks (notably the NAPIS-75) yield a relatively robust chronostratigraphic framework for

central Baffin Bay (from 0 to 115 ka BP). It helps the setting of more precise chronological benchmarks for the dating of major lithological changes and for the BBDC events. It will permit a refinement of paleoceanographic and paleoclimatic interpretations for the late Quaternary depositional history in the bay and thus help identifying ice margin instabilities of the three main regional ice sheets that deliver sediments to the bay. These results also highlight the potential of the paleomagnetic approach to date sedimentary sequence in problematic areas such as Arctic basins.

Acknowledgments

[36] We thank Jacques Labrie (ISMER) for his technical support during paleomagnetic measurements, Louis-Frédéric Daigle (INRS) for the CAT-scan analysis, Pierre Francus (INRS) and Arnaud de Coninck (INRS) for their help during the ITRAX™ core scanning, and Michel Preda (UQAM) for assistance with XRD measurements. Special thanks are due to Olivia Gibb (UQAM) for the picking of the few available foraminifera for ^{14}C ages, to Joseph Stoner (COAS) and Carlos Laj (LSCE) for sharing paleomagnetic data, and John Andrews (INSTAAR) for sharing JR06Bx mineralogical data. We are in debt to Agathe Lisé-Pronovost (ISMER), the anonymous associate editor, two anonymous reviewers and editor-in-chief James Tyburczy for constructive comments that significantly improved the manuscript. We are grateful to the captain, officers, crew and scientists on board the CCGS Hudson during the HU2008-029 expedition. This study is part of the Canadian contribution to the Past4Future project. Support from MDEIE (Ministère du Développement Économique, de l'Innovation et de l'Exportation), NSERC (Natural Sciences and Engineering Research Council of Canada), FQRNT (Fonds Québécois de la Recherche sur la Nature et les Technologies) and the CFI (Canadian Foundation for Innovation) is acknowledged.

References

Aksu, A. E. (1981), Late Quaternary stratigraphy, paleoenvironmentology, and sedimentation history of Baffin Bay and Davis Strait, PhD thesis, Dalhousie Univ., Halifax, Nova Scotia, Canada.

Aksu, A. E. (1983a), Holocene and Pleistocene dissolution cycles in deep-sea cores of Baffin Bay and Davis Strait: Paleoceanographic implications, *Mar. Geol.*, *53*, 331–348, doi:10.1016/0025-3227(83)90049-X.

Aksu, A. E. (1983b), Short-period geomagnetic excursion recorded in Pleistocene sediments of Baffin Bay and Davis Strait, *Geology*, *11*(9), 537–541, doi:10.1130/0091-7613(1983)11<537:SGERIP>2.0.CO;2.

Aksu, A. E., and D. J. W. Piper (1979), Baffin Bay in the past 100,000 yr, *Geology*, *7*, 245–248, doi:10.1130/0091-7613(1979)7<245:BBITPY>2.0.CO;2.

Aksu, A. E., and D. J. W. Piper (1987), Late Quaternary sedimentation in Baffin Bay, *Can. J. Earth Sci.*, *24*, 1833–1846, doi:10.1139/e87-174.

Andrews, J. T., and D. D. Eberl (2011), Surface (sea floor) and near-surface (box cores) sediment mineralogy in Baffin Bay as a key to sediment provenance and ice sheet variations, *Can. J. Earth Sci.*, *48*, 1307–1328, doi:10.1139/e11-021.

Andrews, J. T., A. E. Aksu, M. Kelly, R. Klassen, G. H. Miller, W. N. Mode, and P. Mudie (1985), Land/ocean correlations during the last interglacial/glacial transition, Baffin Bay, northwestern North Atlantic: A review, *Quat. Sci. Rev.*, *4*(4), 333–355, doi:10.1016/0277-3791(85)90005-8.

Andrews, J. T., M. Kirby, A. E. Aksu, D. G. Barber, and D. Meese (1998), Late Quaternary Detrital Carbonate (DC-) layers in Baffin Bay marine sediments (67°–74°N): Correlation with Heinrich events in the North Atlantic?, *Quat. Sci. Rev.*, *17*, 1125–1137, doi:10.1016/S0277-3791(97)00064-4.

Austin, W. E. N., R. J. Telford, U. S. Ninnemann, L. Brown, L. J. Wilson, D. P. Small, and C. L. Bryant (2011), North Atlantic reservoir ages linked to high Younger Dryas atmospheric radiocarbon concentrations, *Global Planet. Change*, *79*(3–4), 226–233, doi:10.1016/j.gloplacha.2011.06.011.

Azetsu-Scott, K., A. Clarke, and K. Falkner (2010), Calcium carbonate saturation states in the waters of the Canadian Arctic Archipelago and the Labrador Sea, *J. Geophys. Res.*, *115*, C11021, doi:10.1029/2009JC005917.

Baldauf, J. G., et al. (1989), Magnetostratigraphic and biostratigraphic synthesis of Ocean Drilling Program Leg 105: Labrador Sea and Baffin Bay, *Proc. Ocean Drill. Program Sci. Results*, *105*, 935–956.

Banerjee, S. K., J. W. King, and J. Marvin (1981), A rapid method for magnetic granulometry with applications to environmental studies, *Geophys. Res. Lett.*, *8*(4), 333–336, doi:10.1029/GL008i004p00333.

Bard, E., M. Arnold, J. Mangeruld, M. Paterne, L. Labeyrie, J. Duprat, M. A. Mélières, E. Sonstegaard, and J. C. Duplessy (1994), The North Atlantic atmosphere-sea surface ^{14}C gradient during the Younger Dryas climatic event, *Earth Planet. Sci. Lett.*, *126*, 275–287, doi:10.1016/0012-821X(94)90112-0.

Blott, S. J., and K. Pye (2001), GRADISTAT: A grain size distribution and statistics package for the analysis of unconsolidated sediments, *Earth Surf. Processes Landforms*, *26*, 1237–1248, doi:10.1002/esp.261.

Bondevik, S., J. Mangerud, H. H. Birks, S. Gulliksen, and P. Reimer (2006), Changes in North Atlantic radiocarbon reservoir ages during the Allerod and Younger Dryas, *Science*, *312*(5779), 1514–1517, doi:10.1126/science.1123300.

Briner, J. P., G. H. Miller, P. T. Davis, P. Bierman, and M. Caffee (2003), Last Glacial Maximum ice sheet dynamics in Arctic Canada inferred from young erratics perched on ancient tors, *Quat. Sci. Rev.*, *22*, 437–444, doi:10.1016/S0277-3791(03)00003-9.

Briner, J. P., G. H. Miller, P. T. Davis, and R. Finkel (2006), Cosmogenic radionuclides from fiord landscapes support differential erosion by overriding ice sheets, *Geol. Soc. Am. Bull.*, *118*, 406–420, doi:10.1130/B25716.1.

Butler, R. F. (1992), *Paleomagnetism: Magnetic Domains to Geologic Terranes*, 319 pp., Blackwell Sci., Oxford, U. K.

Campbell, D. C., and A. de Vernal (2009), CCGS Hudson Expedition 2008029: Marine geology and paleoceanography of Baffin Bay and adjacent areas, Nain, NL to Halifax, NS, August 28-September 23, *Open File 5989*, 212 pp., Geol. Surv. of Can., Ottawa.

Cao, L., R. G. Fairbanks, R. A. Mortlock, and M. J. Risk (2007), Radiocarbon reservoir age of high latitude North Atlantic surface water during the last deglacial, *Quat. Sci. Rev.*, *26*(5–6), 732–742, doi:10.1016/j.quascirev.2006.10.001.

Channell, J. E. T., and C. Xuan (2009), Self-reversal and apparent magnetic excursions in Arctic sediments, *Earth Planet. Sci. Lett.*, *284*(1–2), 124–131, doi:10.1016/j.epsl.2009.04.020.

Channell, J. E. T., D. Hodell, and B. Lehman (1997), Relative geomagnetic paleointensity and $\delta^{18}O$ at ODP Site 983(Gardar Drift, North Atlantic) since 350 ka, *Earth Planet. Sci. Lett.*, *153*, 103–118, doi:10.1016/S0012-821X(97)00164-7.

Channell, J. E. T., A. Mazaud, P. Sullivan, S. Turner, and M. E. Raymo (2002), Geomagnetic excursions and paleointensities in the 0.9–2.15 Ma interval of the Matuyama Chron at Ocean Drilling Program Sites 983 and 984 (Iceland Basin), *J. Geophys. Res.*, *107*(B6), 2114, doi:10.1029/2001JB000491.

Channell, J. E. T., C. Xuan, and D. Hodell (2009), Stacking paleointensity and oxygen isotope data for the last 1.5 Myr (PISO-1500), *Earth Planet. Sci. Lett.*, *283*, 14–23, doi:10.1016/j.epsl.2009.03.012.

Coulthard, R. D., M. F. A. Furze, A. J. Pieńkowski, F. C. Nixon, and J. H. England (2010), New marine Delta R values for Arctic Canada, *Quat. Geochronol.*, *5*, 419–434, doi:10.1016/j.quageo.2010.03.002.

Croudace, I., A. Rindby, and R. Rothwell (2006), ITRAX: Description and evaluation of a new multi-function X-ray core scanner, in *New Techniques in Sediment Core Analysis*, *Geol. Soc. Spec. Publ.*, *267*, 51–63.

Dankers, P. (1981), Relationship between median destructive field and remanent coercive forces for dispersed natural magnetite, titanomagnetite and hematite, *Geophys. J. R. Astron. Soc.*, *64*, 447–461, doi:10.1111/j.1365-246X.1981.tb02676.x.

Day, R., M. D. Fuller, and V. A. Schmidt (1976), Magnetic hysteresis properties of synthetic titanomagnetites, *J. Geophys. Res.*, *81*, 873–880, doi:10.1029/JB081i005p00873.

Day, R., M. D. Fuller, and V. A. Schmidt (1977), Hysteresis properties of titanomagnetites: Grain-size and compositional dependence, *Phys. Earth Planet. Inter.*, *13*, 260–267, doi:10.1016/0031-9201(77)90108-X.

de Vernal, A., C. Hillaire-Marcel, A. E. Aksu, and P. Mudie (1987), Palynostratigraphy and chronostratigraphy of Baffin Bay deep sea cores: Climatostratigraphic implications, *Palaeogeogr. Palaeoclimatol. Palaeoecol.*, *61*, 97–105, doi:10.1016/0031-0182(87)90042-3.

de Vernal, A., G. Bilodeau, C. Hillaire-Marcel, and N. Kassou (1992), Quantitative assessment of carbonate dissolution in marine sediments from foraminifer linings vs. shell ratios: Davis Strait, northwest North Atlantic, *Geology*, *20*, 527–530, doi:10.1130/0091-7613(1992)020<0527:QAOCDI>2.3.CO;2.

Dearing, J. A. (1999), Magnetic susceptibility, in *Environmental Magnetism: A Practical Guide*, edited by J. Walden, F. Oldfiel, and J. P. Smith, pp. 35–53, Quat. Res. Assoc., London.

Duchesne, M., F. Moore, B. Long, and J. Labrie (2009), A rapid method for converting medical Computed Tomography scanner topogram attenuation scale to Hounsfield Unit scale and to obtain relative density values, *Eng. Geol. Amsterdam*, *103*, 100–105, doi:10.1016/j.enggeo.2008.06.009.

Dunlop, D. J. (2002a), Theory and application of the Day plot (M_{rs}/M_s versus H_{cr}/H_c): 1. Theoretical curves and tests using titanomagnetite data, *J. Geophys. Res.*, *107*(B3), 2056, doi:10.1029/2001JB000486.

Dunlop, D. J. (2002b), Theory and application of the Day plot (M_{rs}/M_s versus H_{cr}/H_c): 2. Application to data for rocks, sediments, and soils, *J. Geophys. Res.*, *107*(B3), 2057, doi:10.1029/2001JB000487.

Dunlop, D. J., and Ö. Özdemir (1997), *Rock Magnetism: Fundamentals and Frontiers*, Cambridge Univ. Press, New York, doi:10.1017/CBO9780511612794.

Dunlop, D. J., and Ö. Özdemir (2007), Magnetizations in rocks and minerals, in *Treatise on Geophysics*, vol. 5, *Geomagnetism*, edited by G. Schubert, pp. 277–336, Elsevier, Amsterdam, doi:10.1016/B978-044452748-6.00093-6.

Dyke, A. (2004), An outline of North American deglaciation with emphasis on central and northern Canada, *Dev. Quat. Sci.*, *2*, 373–424, doi:10.1016/S1571-0866(04)80209-4.

England, J., N. Atkinson, J. Bednarski, A. Dyke, D. A. Hodgson, and C. O'Cofaigh (2006), The Innuitian Ice Sheet: Configuration, dynamics and chronology, *Quat. Sci. Rev.*, *25*, 689–703, doi:10.1016/j.quascirev.2005.08.007.

Funder, S., K. K. Kjeldsen, K. H. Kjær, and C. Ó. Cofaigh (2011), The Greenland Ice Sheet during the past 300,000 years: A review, in *Quaternary Glaciations, Extent and Chronology, Part IV, A Closer Look*, *Dev. Quat. Sci.*, vol. 15, edited by J. Ehlers, P. L. Gibbard, and P. D. Hughes, pp. 699–713, Elsevier, Amsterdam, doi:10.1016/B978-0-444-53447-7.00050-7.

Guyodo, Y., and J. P. Valet (1996), Relative variations in geomagnetic intensity from sedimentary records: The past 200,000 years, *Earth Planet. Sci. Lett.*, *143*, 23–36, doi:10.1016/0012-821X(96)00121-5.

Hillaire-Marcel, C., and A. de Vernal (2008), Stable isotope clue to episodic sea ice formation in the glacial North Atlantic, *Earth Planet. Sci. Lett.*, *268*, 143–150, doi:10.1016/j.epsl.2008.01.012.

Hillaire-Marcel, C., A. de Vernal, A. E. Aksu, and S. Macko (1989), High-resolution isotopic and micropaleontological studies of upper Pleistocene sediment at ODP site 645, Baffin Bay, *Proc. Ocean Drill. Program Sci. Results*, *105*, 599–616, doi:10.2973/odp.proc.sr.105.138.1989.

Hillaire-Marcel, C., A. de Vernal, L. Polyak, and D. A. Darby (2004), Size-dependent isotopic composition of planktic foraminifers from Chukchi Sea vs. NW Atlantic sediments—Implications for the Holocene paleoceanography of the western Arctic, *Quat. Sci. Rev.*, *23*, 245–260, doi:10.1016/j.quascirev.2003.08.006.

Hiscott, R. N., A. E. Aksu, and O. B. Nielsen (1989), Provenance and dispersal patterns, Pliocene-Pleistocene section at site 645, Baffin Bay, *Proc. Ocean Drill. Program Sci. Results*, *105*, 31–52, doi:10.2973/odp.proc.sr.105.117.1989.

Hughen, K., S. Lehman, J. Southon, J. T. Overpeck, O. Marchal, C. Herring, and J. Turnbull (2004), ^{14}C activity and global carbon cycle changes over the past 50,000 years, *Science*, *303*(5655), 202–207, doi:10.1126/science.1090300.

Jennings, A. E., C. Sheldon, T. M. Cronin, P. Francus, J. Stoner, and J. T. Andrews (2011), The Holocene history of Nares Strait: Transition from glacial bay to Arctic-Atlantic throughflow, *Oceanography*, *24*(3), 26–41, doi:10.5670/oceanog.2011.52.

King, J., S. K. Banerjee, J. Marvin, and Ö. Özdemir (1982), A comparison of different magnetic methods for determining the relative grain size of magnetite in natural materials: Some results from lake sediments, *Earth Planet. Sci. Lett.*, *59*, 404–419, doi:10.1016/0012-821X(82)90142-X.

King, J., S. K. Banerjee, and J. Marvin (1983), A new rock-magnetic approach to selecting sediments for geomagnetic paleointensity studies: Application to paleointensity for the last 4000 years, *J. Geophys. Res.*, *88*(B7), 5911–5921, doi:10.1029/JB088iB07p05911.

Kirschvink, J. L. (1980), The least-squares line and plane and the analysis of palaeomagnetic data, *Geophys. J. R. Astron. Soc.*, *62*, 699–718, doi:10.1111/j.1365-246X.1980.tb02601.x.

Kissel, C., C. Laj, L. Labeyrie, T. Dokken, A. Voelker, and D. Blamart (1999), Rapid climatic variations during marine isotopic stage 3: Magnetic analysis of sediments from Nordic Seas and North Atlantic, *Earth Planet. Sci. Lett.*, *171*, 489–502, doi:10.1016/S0012-821X(99)00162-4.

Korstgård, J. A., and O. B. Nielsen (1989), Provenance of dropstones in Baffin Bay and Labrador Sea, *Proc. Ocean Drill. Program Sci. Results*, *105*, 65–69, doi:10.2973/odp.proc.sr.105.200.1989.

Laj, C., and J. E. T. Channell (2007), Geomagnetic excursions, in *Treatise on Geophysics*, vol. 5, *Geomagnetism*, edited by G. Schubert, pp. 373–416, Elsevier, Amsterdam, doi:10.1016/B978-044452748-6.00095-X.

Laj, C., C. Kissel, A. Mazaud, J. E. T. Channell, and J. Beer (2000), North Atlantic palaeointensity stack since 75 ka (NAPIS-75) and the duration of the Laschamp event, *Philos. Trans. R. Soc. London, Ser. B*, *358*, 1009–1025, doi:10.1098/rsta.2000.0571.

Laj, C., C. Kissel, and A. P. Roberts (2006), Geomagnetic field behavior during the Iceland Basin and Laschamp geomagnetic excursions: A simple transitional field geometry?, *Geochem. Geophys. Geosyst.*, *7*, Q03004, doi:10.1029/2005GC001122.

Levi, S., and S. K. Banerjee (1976), On the possibility of obtaining relative paleointensities from lake sediments, *Earth Planet. Sci. Lett.*, *29*, 219–226, doi:10.1016/0012-821X(76)90042-X.

Lund, S. P., M. Schwartz, L. Keigwin, and T. Johnson (2005), Deep-sea sediment records of the Laschamp geomagnetic field excursion (~41,000 calendar years before present), *J. Geophys. Res.*, *110*, B04101, doi:10.1029/2003JB002943.

Lund, S. P., J. S. Stoner, J. E. T. Channell, and G. Acton (2006), A summary of Brunhes paleomagnetic field variability recorded in Ocean Drilling Program cores, *Phys. Earth Planet. Inter.*, *156*, 194–204, doi:10.1016/j.pepi.2005.10.009.

MacLean, B. (1985), Geology of the Baffin Island Shelf, in *Quaternary Environments: Eastern Canadian Arctic, Baffin Bay and Western Greenland*, edited by J. T. Andrews, pp. 154–177, Allen and Unwin, Boston.

MacLean, B., G. L. Williams, and S. P. Srivastava (1990), Geology of Baffin Bay and Davis Strait, in *Geology of Canada*, vol. 2, *Geology of the Continental Margin of Eastern Canada*, edited by M. J. Keen and G. L. Williams, pp. 293–348, Geol. Surv. of Can., Ottawa.

Maher, B. A., and R. Thompson (Eds.) (1999), *Quaternary Climates, Environments and Magnetism*, Cambridge Univ. Press, Cambridge, U. K., doi:10.1017/CBO9780511535635.

Marlowe, J. I. (1966), Mineralogy as an indicator of long-term current fluctuations in Baffin Bay, *Can. J. Earth Sci.*, *3*(2), 191–201, doi:10.1139/e66-015.

Mazaud, A. (2005), User-friendly software for vector analysis of the magnetization of long sediment cores, *Geochem. Geophys. Geosyst.*, *6*, Q12006, doi:10.1029/2005GC001036.

Meynadier, L., J. P. Valet, and R. Weeks (1992), Relative geomagnetic intensity of the field during the last 140 ka, *Earth Planet. Sci. Lett.*, *114*(1), 39–57, doi:10.1016/0012-821X(92)90150-T.

Moskowitz, B. (1991), Hitchhiker's guide to magnetism, in *Environmental Magnetism Workshop (IRM)*, vol. 279(1), 48 pp., Inst. for Rock Magnetism, Univ. of Minn., Minneapolis.

Mudie, P., and A. E. Aksu (1984), Palaeoclimate of Baffin Bay from 300,000-year record of foraminifera, dinoflagellates and pollen, *Nature*, *312*, 630–634, doi:10.1038/312630a0.

O'Cofaigh, C., et al. (2010), West Greenland ice streams on the continental shelf of Baffin Bay during the Last Glacial Cycle: Geomorphology, flow trajectories and chronology, paper presented at 40th Arctic Workshop, Inst. of Arctic and Alpine Res., Univ. of Colo., Winter Park, Colo.

Opdyke, N. D., and J. E. T. Channell (1996), *Magnetic Stratigraphy*, Academic, San Diego, Calif.

Paillard, D., L. Labeyrie, and P. Yiou (1996), Macintosh program performs time-series analysis, *Eos Trans. AGU*, *77*(39), 379, doi:10.1029/96EO00259.

Parnell, J., S. Bowden, J. T. Andrews, and C. Taylor (2007), Biomarker determination as a provenance tool for detrital carbonate events (Heinrich events?): Fingerprinting Quaternary glacial sources into Baffin Bay, *Earth Planet. Sci. Lett.*, *257*, 71–82, doi:10.1016/j.epsl.2007.02.021.

Piper, D. J. W. (1973), A late quaternary stratigraphic marker in the Central Basin of Baffin Bay, *Marit. Sediments*, *9*, 62–63.

Polyak, L., et al. (2009), Late Quaternary stratigraphy and sedimentation patterns in the western Arctic Ocean, *Global Planet. Change*, *68*, 5–17, doi:10.1016/j.gloplacha.2009.03.014.

Reimer, P. J., et al. (2009), Intcal09 and Marine09 radiocarbon age calibration curves, 0–50,000 years cal BP, *Radiocarbon*, *51*(4), 1111–1150.

Roberts, A. P. (2008), Geomagnetic excursions: Knowns and unknowns, *Geophys. Res. Lett.*, *35*, L17307, doi:10.1029/2008GL034719.

Roberts, A. P., L. Chiang, C. J. Rowan, C.-S. Horng, and F. Florindo (2011), Magnetic properties of sedimentary Greigite (Fe_3S_4): An update, *Rev. Geophys.*, *49*, RG1002, doi:10.1029/2010RG000336.

Spassov, S., and J.-P. Valet (2012), Detrital magnetizations from redeposition experiments of different natural sediments, *Earth Planet. Sci. Lett.*, *351–352*, 147–157, doi:10.1016/j.epsl.2012.07.016.

Srivastava, S. P., et al. (1989), *Proceedings of the Ocean Drilling Program, Scientific Results*, vol. 105, Ocean Drill. Program, College Station, Tex.

Stoner, J. S., and G. St-Onge (2007), Magnetic stratigraphy in paleoceanography: Reversals, excursions, paleointensity and secular variation, in *Developments in Marine Geology*, vol. 1, *Proxies in Late Cenozoic Paleoceanography*, edited by C. Hillaire-Marcel and A. de Vernal, pp. 99–138, Elsevier, Amsterdam, doi:10.1016/S1572-5480(07)01008-1.

Stoner, J. S., J. E. T. Channell, and C. Hillaire-Marcel (1996), The magnetic signature of rapidly deposited detrital layers from the deep Labrador Sea: Relationship to North Atlantic Heinrich layers, *Paleoceanography*, *11*, 309–325, doi:10.1029/96PA00583.

Stoner, J. S., J. E. T. Channell, and C. Hillaire-Marcel (1998), A 200 ka geomagnetic chronostratigraphy for the Labrador Sea: Indirect correlation of the sediment record to SPECMAP, *Earth Planet. Sci. Lett.*, *159*, 165–181, doi:10.1016/S0012-821X(98)00069-7.

Stoner, J. S., J. E. T. Channell, C. Hillaire-Marcel, and C. Kissel (2000), Geomagnetic paleointensity and environmental record from Labrador Sea core MD95-2024: Global marine sediment and ice core chronostratigraphy for the last 110 kyr, *Earth Planet. Sci. Lett.*, *183*, 161–177, doi:10.1016/S0012-821X(00)00272-7.

St-Onge, G., and J. S. Stoner (2011), Paleomagnetism near the North Magnetic Pole: A unique vantage point to understand

the dynamics of the geomagnetic field and its secular variations, *Oceanography*, *24*(3), 42–50, doi:10.5670/oceanog.2011.53.

St-Onge, G., T. Mulder, P. Francus, and B. Long (2007), Continuous physical properties of cored marine sediments, in *Developments in Marine Geology*, vol. 1, *Proxies in Late Cenozoic Paleoceanography*, edited by C. Hillaire-Marcel and A. de Vernal, pp. 63–98, Elsevier, Amsterdam, doi:10.1016/S1572-5480(07)01007-X.

Stuiver, M., and H. A. Polach (1977), Discussion: Reporting of ^{14}C data, *Radiocarbon*, *19*, 355–363.

Stuiver, M., P. J. Reimer, and R. W. Reimer (2010), CALIB 6.0, program, Queens Univ., Belfast, U. K. [Available at http://radiocarbon.pa.qub.ac.uk/calib/.]

Tang, C., C. Ross, T. Yao, B. Petrie, B. DeTracey, and E. Dunlap (2004), The circulation, water masses and sea-ice of Baffin Bay, *Prog. Oceanogr.*, *63*, 183–228, doi:10.1016/j.pocean.2004.09.005.

Tauxe, L. (1993), Sedimentary records of relative paleointensity of the geomagnetic field: Theory and practice, *Rev. Geophys.*, *31*, 319–354, doi:10.1029/93RG01771.

Tauxe, L. (2010), *Essentials of Paleomagnetism*, Univ. of Calif. Press, San Diego.

Tauxe, L., and G. Wu (1990), Normalized remanence in sediments of the western equatorial Pacific: Relative paleointensity of the geomagnetic field?, *J. Geophys. Res.*, *95*(B8), 12,337–12,350, doi:10.1029/JB095iB08p12337.

Tauxe, L., and T. Yamazaki (2007), Paleointensities, in *Treatise on Geophysics*, vol. 5, *Magnetism*, edited by G. Schubert, pp. 509–563, Elsevier, Amsterdam, doi:10.1016/B978-044452748-6.00098-5.

Tauxe, L., T. Mullender, and T. Pick (1996), Potbellies, wasp-waists, and superparamagnetism in magnetic hysteresis, *J. Geophys. Res.*, *101*, 571–583, doi:10.1029/95JB03041.

Thiébault, F., M. Cremer, P. Debrabant, J. Foulon, O. B. Nielsen, and H. Zimmerman (1989), Analysis of sedimentary facies, clay mineralogy, and geochemistry of the Neogene-Quaternary sediments in Site 645, Baffin Bay, *Proc. Ocean Drill. Program Sci. Results*, *105*, 83–100, doi:10.2973/odp.proc.sr.105.111.1989.

Thorez, J. (2003), L'argile, minéral pluriel, *Bull. Soc. R. Sci. Liège*, *72*(1), 19–70.

Thouveny, N. (1988), High-resolution palaeomagnetic study of Late Pleistocene sediments from Baffin Bay: First results, *Can. J. Earth Sci.*, *25*, 833–843, doi:10.1139/e88-082.

Valet, J. P. (2003), Time variations in geomagnetic intensity, *Rev. Geophys.*, *41*(1), 1004, doi:10.1029/2001RG000104.

Vincent, J., and V. Prest (1987), The early Wisconsinan history of the Laurentide ice sheet, *Géogr. Phys. Quat.*, *41*, 199–213.

Waelbroeck, C., J. C. Duplessy, E. Michel, L. Labeyrie, D. Paillard, and J. Duprat (2001), The timing of the last deglaciation in North Atlantic climate records, *Nature*, *412*, 724–727, doi:10.1038/35089060.

Xuan, C., and J. E. T. Channell (2010), Origin of apparent magnetic excursions in deep-sea sediments from Mendeleev-Alpha Ridge, Arctic Ocean, *Geochem. Geophys. Geosyst.*, *11*, Q02003, doi:10.1029/2009GC002879.

Xuan, C., J. E. T. Channell, L. Polyak, and D. A. Darby (2012), Paleomagnetism of Quaternary sediments from Lomonosov Ridge and Yermak Plateau: Implications for age models in the Arctic Ocean, *Quat. Sci. Rev.*, *32*, 48–63, doi:10.1016/j.quascirev.2011.11.015.

Zijderveld, J. D. A. (1967), AC demagnetization of rock: Analysis of results, in *Methods in Paleomagnetism*, edited by D. W. Collinson, K. M. Creer, and S. K. Runcorn, pp. 254–286, Elsevier, Amsterdam.